Author: Karska, Agata
Title: Feedback from deeply embedded low- and high-mass protostars. Surveying hot molecular gas with Herschel
Issue Date: 2014-09-24

5

Physics of deeply-embedded low-mass protostars: evolution of shocks, ultraviolet radiation, and mass flux rates

A. Karska, E. F. van Dishoeck, N. J. Evans II, L. E. Kristensen, J. C. Mottram,
J. D. Green, G. J. Herczeg, J. K. Jørgensen, and DIGIT, WISH, and WILL teams

To be submitted to *Astrophysical Journal Supplement Series*

Abstract

During the embedded phase of the protostellar evolution, the dense envelope is partly accreted onto the protostar and partly dispersed by the outflow. Far-infrared molecular and atomic lines are unique diagnostics of the physical conditions, outflow shocks and ultraviolet radiation needed to understand the physics of the accretion and dispersal process. We used *Herschel* / PACS to obtain spectral maps of 90 nearby ($D \lesssim 450$ pc) low-mass protostars at 55-210 μm as part of the ‘Water in Star Forming Regions with Herschel’ (WISH), ‘William Herschel Line Legacy’ (WILL), and ‘Dust, Ice, and Gas in Time’ (DIGIT) surveys. The maps show typically compact (~1000 AU scales) emission in CO, H_2O, and OH lines, and more extended (up to ~10,000 AU) emission in [O I] and [C II] lines.

Rich molecular spectra are detected towards 70 out of 90 sources, including 27 sources with the detection of the highly-excited H_2O 8_{18}-7_{07} line (E_u/k_B = 1071 K) and highly-excited CO ($J_{up} \gtrsim 30$) emission. Similar to previous studies, two components are found on CO rotational diagrams corresponding to median rotational temperatures of ~ 320 K and ~ 690 K. Detection of highly-excited CO and H_2O lines and analysis of CO rotational diagrams indicate an origin in hot ($T \gtrsim 300$ K) and dense ($n \gtrsim 10^4$ cm^{-3}) gas. Non-dissociative shocks can reproduce the observed molecular emission, but additional dissociative shocks and / or ultraviolet radiation (UV) are needed to account for the [O I] and some of the OH emission. The [C II] emission cannot be reproduced by any shock model and, when spatially associated with a young stellar object, characterizes the hard ultraviolet radiation (λ <1100 Å) from the protostar. For the few sources where this line is detected, incident radiation fields $G \sim 10-100$ G_0 are found, in agreement with UV fields employed in recent models of UV irradiated cavities (Visser et al. 2012). Inferred densities of $n \sim 10^4 - 10^{5.5}$ cm^{-3} for the PDR layer are an order of magnitude lower than those obtained independently from shock models, suggesting the origin of [C II] emission is in the jet and not the outflow cavity walls.

The decrease of the H_2O / OH intensity ratio from Class 0 to Class I stages provides direct evidence for an increasing role of UV radiation as the protostar evolves. Such a trend is not found for the H_2O / [O I] ratio, most probably due to the larger contribution from the jet to the [O I] emission in the dense envelopes of Class 0 sources. Mass flux rates of dM_w/dt ~ 10^{-8} $M_\odot$ yr^{-1} are determined from the [O I] line, on the assumption that most of the [O I] emission originates solely in the dissociative jet shock, which we argue is not the case so these values are in fact upper limits. Nevertheless, these rates are up to about an order of magnitude lower than those determined for the entrained outflow gas from the CO 3-2 and CO 6-5 maps, especially for the most deeply embedded sources. In contrast, Class I sources show lower CO / [O I] mass flux rates than the Class 0 sources, suggesting that the jet evolves from molecular to atomic form during the embedded phase.

5.1 Introduction

Complex physical processes are at play during the earliest, deeply-embedded stage of low-mass star formation. A fraction of the dense envelope material is accreted onto the protostar, but part of it is also removed in the form of collimated jets that entrain the surrounding material and produce wider-angle outflows. The envelope is partially emptied in the outflow cones allowing ultraviolet (UV) photons from a protostar to reach the 'cavity walls'. The 'bow shock', at the tip of the jet, is strong enough to produce additional UV that heats the cavities. The interplay of these processes makes it difficult to characterize them individually and track their evolution from the Class 0 to I stages.

The common signature of these processes is a presence of hot ($T \gtrsim 300$ K) and dense ($n \gtrsim 10^4$ cm^{-3}) gas that cools via emission lines of hydrogen (H_2), water vapor (H_2O), carbon monoxide (CO), hydroxyl (OH), atomic oxygen ([O I]), and ionized carbon ([C II]) at far-infrared wavelengths (Hollenbach et al. 1989). Observed intensities of those lines and their line ratios are therefore useful diagnostics of shocks and photodissociation regions (PDRs) produced in the young stellar object (YSO) environment. In particular, the type of shock, its velocity, and the pre-shock density of the ambient medium can be obtained from comparisons to detailed shock models (e.g. Kaufman & Neufeld 1996, Flower & Pineau des Forêts 2010, 2012). Independent measures of the gas density and the incident UV field in a YSO can be derived from the PDR models (e.g. Kaufman et al. 1999), but the shocks and large-scale cloud PDR contribution to the emission lines need to be first subtracted.

First far-infrared (IR) spectra of low-mass YSOs were obtained with Long-Wavelength Spectrometer onboard the *Infrared Space Observatory* (Kessler et al. 1996, Clegg et al. 1996). The main shortcoming of those early observations was the large telescope beam ($\sim 80''$) and thus the contamination from the cloud PDR emission and from multiple sources and / or outflows. Nevertheless, a few pointed observations of L1448 allowed to associate the far-IR line emission with the H_2 and low-J CO outflow (Nisini et al. 2000). A combination of a slow, non-dissociative shock and a fast, dissociative shock from the jet was then invoked to explain the observed molecular and [O I] emission, respectively (Giannini et al. 2001, Nisini et al. 2002b). A survey of 28 Class 0/I protostars revealed a gradual decrease in the molecular emission and an increase in the [O I] emission, attributed to the weakening of shocks and less-shielded UV for the less-massive envelopes of more evolved sources. For the Class 0 sources, however, the [O I] emission was linked only to jet shocks, and as such was used to derive mass loss rates (denoted here as mass flux rates). Giannini et al. (2001) found agreement between those rates and the CO mass flux tracing the entrained outflow activity over much longer periods and suggested that the mass flux rate, and thus the accretion, occur at a constant pace during the protostellar phase.

Far-IR spectral maps from the Photodetector Array Camera and Spectrometer (PACS) (Poglitsch et al. 2010) on board the *Herschel* Space Observatory (Pilbratt et al. 2010a)[1]

---

[1] Herschel is an ESA space observatory with science instruments provided by European-led Principal Investigator consortia and with important participation from NASA.

are well-suited to revisit the *ISO*/LWS results due to enhanced sensitivity, along with improved spatial and spectral resolution. The array of 5×5 elements covers a total field of view of $\sim 47''$ with $9.4''$ pixels, corresponding to the spatial resolution scales of order ~ 1000 AU at distances to the nearby protostars ($D \sim 200$ pc).

The PACS maps obtained as part of the 'Water in Star forming regions with Herschel' (WISH) survey show extended molecular and [O I] emission along the outflow direction in half of the 18 targeted sources and [C II] emission associated with a cloud PDR (van Dishoeck et al. 2011, Nisini et al. 2010a, Karska et al. 2013, Santangelo et al. 2013). In the 'Dust, Ice, and Gas in Time' survey of 30 protostars, much more compact emission was detected, implying that the extended emission is not a common characteristics of Class 0/I YSOs (Green et al. 2013). At the same time, CO rotational diagrams in all those sources show surprisingly similar two temperature components, with $T_{\rm rot} \sim 300$ K and $\gtrsim 700$ K, irrespective of the protostellar luminosity, envelope mass, and evolutionary stage (see also Goicoechea et al. 2012, Herczeg et al. 2012, Lindberg et al. 2013, van der Marel et al. 2013). CO ladders for small subsamples of sources have been modeled with a combination of non-dissociative shocks and UV heating along the cavity wall (van Kempen et al. 2010b, Visser et al. 2012), but an equally good solution was obtained by invoking two shocks alone (Flower & Pineau des Forêts 2013). The argument in favor of a hot component arising in the slow dissociative shock was put forward by Kristensen et al. (2013), who linked the hotter component with a kinematic component extracted from velocity-resolved H_2O profiles of the same protostars observed with the Heterodyne Instrument for the Far-Infrared (HIFI; de Graauw et al. 2010).

A systematic comparison of *Herschel* / PACS spectra of 22 protostars in Perseus with shock models from Kaufman & Neufeld (1996) and Flower & Pineau des Forêts (2010) was presented in Karska et al. (subm.). Line ratios of various CO, and separately H_2O lines, show good agreement with non-dissociative shock models with pre-shock densities of $\sim 10^5$ cm^{-3} and shock velocities of $\gtrsim 20$ km s^{-1}. However, the models used for those comparisons overproduced by 1-2 orders of magnitude the H_2O / CO and H_2O / OH line ratios, indicating that the inclusion of shock illumination by ultraviolet photons is needed. The presence of irradiated shocks is also invoked to explain the complex H_2O spectra from HIFI, with the 'broad' and 'offset' components linked to irradiated $C-$type and $J-$type shocks, respectively (Kristensen et al. 2013, Suutarinen et al. 2014, Mottram et al. subm.). Since the $J-$type dissociative shocks contribute only a small fraction of the flux to the CO lines with $J \lesssim 30$, a larger number of sources with even higher$-J$ CO lines is needed to study this component with PACS.

To address those issues, a consistent analysis of a large and uniform sample of protostars is clearly needed. In this paper, the WISH and DIGIT sources are re-analyzed together with an additional 50 sources observed as part of the 'William Herschel Line Legacy' survey (WILL, Mottram et al. in prep.) to answer the following questions: What determines the detection of highly-excited CO and spatially-extended line emission? What are the typical spatial scales of line emission? Do line fluxes of different species correlate with each other? What part of the [O I] and [C II] emission originates in the YSOs and can be attributed to the shock and / or PDR components? Do total molecular and atomic cooling rates change from the Class 0 to Class I stage? What are the implications for the mass flux rates calculated from the [O I] line and how do they compare with the mass flux rates based on CO outflows?

This paper is organized as follows. Section 2 describes our sample selection, observations, and data reduction. §3 compiles results on detection statistics and cross-species line correlations. §4 shows analysis of CO excitation, molecular and atomic cooling, and mass loss rates, and how they evolve from Class 0 to I phase. Comparison of absolute line emission of [O I] and [C II] lines to shock and photodissociation regions models is presented. §5 discusses the results obtained in §3 and §4 and §6 presents the summary and conclusions.

5.2 Observations

5.2.1 Sample selection

The low-mass embedded protostars analyzed here were initially observed as part of the 'Water In Star forming regions with Herschel' (WISH, van Dishoeck et al. 2011) and 'Dust, Ice, and Gas In Time' (DIGIT, Green et al. 2013) surveys, comprised of 18 and 29 Class 0/I protostars targeted with PACS, respectively, including 8 overlap sources. This sample was subsequently enlarged by the 'William Herschel Line Legacy' survey (WILL, Mottram et al. in prep.), where an additional 50 Class 0/I sources were observed, including 2 sources in common with the WISH and DIGIT programs. Three more sources were further extracted from the PACS spectral maps of the primary targets (ID numbers 4, 82, 85), increasing the sample to 90 sources in total (for details, see Table 5.1). Most of our sources are located in Perseus (30 sources), Taurus (12 sources), Ophiuchus (9 sources), Aquila Rift complex (6 sources in Aquila, 7 sources in W40, and 2 sources in Serpens South), Corona Australis (5 sources), and Serpens (3 sources) molecular clouds, at distances $\lesssim$ 450 pc (for distance references see Kristensen et al. 2012, Green et al. 2013, Mottram et al. in prep.).

The selection procedure for the WISH and DIGIT sources are discussed in detail in van Dishoeck et al. (2011) and Green et al. (2013), with a general rule that all of them are well-known and extensively studied protostars. The WILL sources were selected based on unbiased mid-IR and millimeter continuum observations with *Spitzer* and various ground-based telescopes. Protostars in Perseus and Ophiuchus were selected from the 'Cores to Disk' program (c2d, Evans et al. 2009), and extensively discussed in Jørgensen et al. (2007a) and Rebull et al. (2007) (Perseus) and in Jørgensen et al. (2008) (Ophiuchus), with (sub-)millimeter follow-up in Enoch et al. (2009), van Kempen et al. (2009c), and van der Marel et al. (2013). Protostars in Taurus were observed as part of the 'Taurus Spitzer Survey' and catalogued in Rebull et al. (2010). Corona Australis (CrA 1) and Ophiuchus North / Scorpius (Sco1) protostars are from the 'Spitzer Gould Belt Survey' (Peterson et al. 2011, Hatchell et al. 2012). Sources located in the Aquila Rift complex (Gutermuth et al. 2008) are catalogued in Maury et al. (2011). The details will be discussed in Mottram et al. in prep.

The entire sample of protostars covers a broad range of bolometric temperatures and

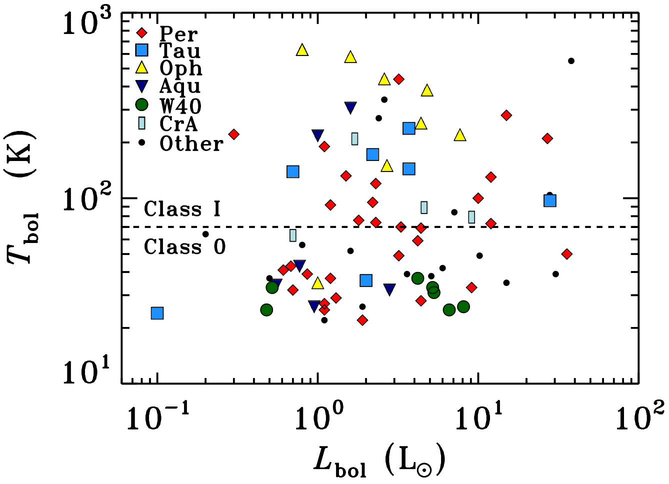

Figure 5.1 – T_{bol} – L_{bol} diagram illustrating the variety of physical parameters determined for the protostars from our survey. Protostars in Perseus, Taurus, Ophiuchus, Aquila, W40, and CrA are showed in red diamonds, blue squares, yellow triangles, navy rotated triangles, green circles, and light blue rectangles, respectively.

luminosities (Table 5.1), with specific clouds often located at selected parts of the T_{bol} – L_{bol} diagram, as illustrated in Figure 5.1. The most luminous protostars are those in Perseus and Taurus, with average bolometric luminosities of 5 – 6 $L_\odot$, whereas the sources in Aquila have on average the lowest luminosities, ~ 1.3 $L_\odot$. Bolometric temperatures are the lowest for the Serpens and W40 protostars (average T_{bol} of ~ 30 K) and the highest for Ophiuchus protostars (~ 370 K). The average bolometric temperature for the rest of the clouds is around 100 K. In total, 45 Class 0 (T_{bol} 70 K) and 45 Class I ($T_{\mathrm{bol}} > 70$ K and 650 K) sources were observed.

Table 5.1 – Bolometric Temperatures, Luminosities, and Envelope Masses of Embedded Protostars

ID	Position	Cloud	Dist. (pc)	$T_{\rm bol}$ (K)	$L_{\rm bol}$ ($L_\odot$)	$M_{\rm env}$[a] ($M_\odot$)	Region	Other names	Project[b]
1	03:25:22.33 +30:45:14.0	Per	235	74	2.3	1.1	L1448	Per-emb 22, YSO 1, L1448 IRS2, I03222+3034	WILL (Per01)
2	03:25:36.48 +30:45:22.3	Per	235	73	12	3.2	L1448	Per-emb 33, YSO 2, L1448 N(A), L1448 IRS3	WILL (Per02)
3	03:25:38.82 +30:44:06.3	Per	235	69	4.4	3.9	L1448	Per-emb 26, YSO 3, L1448 C(S)	DIGIT
4	03:25:39.10 +30:43:58.0	Per	235	190	1.1	2.6	L1448	Per-emb 42, YSO 3, L1448 MMS, L1448 C(N)	DIGIT (Per03)
5	03:26:37.46 +30:15:28.0	Per	235	92	1.2	0.3	L1451	Per-emb 25, YSO 4, I03235+3004	WILL (Per04)
6	03:27:39.09 +30:13:03.0	Per	235	59	4.2	–	L1455	Per-emb 17, YSO 6, I03245+3002, L1455-IRS1	DIGIT
7	03:28:00.40 +30:08:01.3	Per	235	221	0.3	–	L1455	Per-emb 46, L1455-IRS3, I03249+2957	DIGIT
8	03:28:37.09 +31:13:30.7	Per	235	130	12	0.4	NGC1333	Per-emb 35, YSO 11, NGC1333 I1, I03255+3103	WILL (Per05)
9	03:28:55.56 +31:14:36.6	Per	235	50	35.7	5.1	NGC1333	Per-emb 27, YSO 15, NGC1333 I2A	WISH
10	03:28:57.36 +31:14:15.7	Per	235	100	10	0.3	NGC1333	Per-emb 36, YSO 16, NGC1333 I2B	WILL (Per06)
11	03:29:00.52 +31:12:00.7	Per	235	32	0.7	0.3	NGC1333	Per-emb 3, YSO 18, HRF 65	WILL (Per07)
12	03:29:01.57 +31:20:20.7	Per	235	280	15	0.9	NGC1333	Per-emb 54, YSO 19, HH 12	WILL (Per08)
13	03:29:07.76 +31:21:57.2	Per	235	210	27	0.2	NGC1333	Per-emb 50	WILL (Per09)
14	03:29:10.50 +31:13:31.0	Per	235	33	9.1	5.6	NGC1333	Per-emb 12, YSO 22, NGC1333 I4A	WISH
15	03:29:10.68 +31:18:20.5	Per	235	70	3.3	1.4	NGC1333	Per-emb 21, YSO 23, HRF 46	WILL (Per10)
16	03:29:12.04 +31:13:01.5	Per	235	28	4.4	3.0	NGC1333	Per-emb 13, YSO 25, NGC1333 I4B	WISH (Per11)
17	03:29:13.52 +31:13:58.0	Per	235	39	0.9	1.3	NGC1333	Per-emb 14, YSO 26, NGC1333 I4C	WILL (Per12)
18	03:29:51.82 +31:39:06.1	Per	235	41	0.6	0.5	NGC1333	Per-emb 9, YSO 31, I03267+3128	WILL (Per13)
19	03:30:15.12 +30:23:49.2	Per	235	120	2.3	0.1	B1-ridge	Per-emb 34, I03271+3013	WILL (Per14)
20	03:31:20.96 +30:45:30.2	Per	235	37	1.2	1.3	B1-ridge	Per-emb 5, YSO 32, I03282+3035	WILL (Per15)
21	03:32:17.95 +30:49:47.6	Per	235	29	1.3	2.8	B1-ridge	Per-emb 2, YSO 33, I03292+3039	WILL (Per16)
22	03:33:12.85 +31:21:24.1	Per	235	438	3.2	–	B1	Per-emb 64, I03301+3111, Bolo76	DIGIT
23	03:33:14.40 +31:07:10.9	Per	235	43	0.7	1.2	B1	Per-emb 6, YSO 35, B1 SMM3	WILL (Per17)
24	03:33:16.45 +31:06:52.5	Per	235	25	1.1	1.2	B1	Per-emb 10, YSO 36, B1 d	WILL (Per18)
25	03:33:16.66 +31:07:55.2	Per	235	132	1.5	–	B1	Per-emb 40, YSO 37, B1 a, I03301+3057	DIGIT
26	03:33:17.85 +31:09:32.0	Per	235	76	1.8	–	B1	Per-emb 29, YSO 38, B1 c	DIGIT
27	03:33:27.28 +31:07:10.2	Per	235	95	2.2	0.2	B1	Per-emb 30, YSO 40, B1 SMM11	WILL (Per19)
28	03:43:56.53 +32:00:52.9	Per	235	22	1.9	2.1	IC 348	Per-emb 1, YSO 44, HH 211 MMS	WILL (Per20)
29	03:43:56.85 +32:03:04.6	Per	235	27	1.1	1.9	IC 348	Per-emb 11, YSO 43, IC348 MMS, IC348 SW	WILL (Per21)
30	03:44:43.94 +32:01:36.1	Per	235	49	3.2	0.6	IC 348	Per-emb 8, YSO 48, IC348 a, I03415+3152	WILL (Per22)
31	04:04:42.9 +26:18:56.3	Tau	140	238	3.7	0.2		L1489	DIGIT/WISH
32	04:19:58.4 +27:09:57.0	Tau	140	131	1.5	0.3		I04169+2702	WILL (Tau01)

Continued on next page

Table 5.1 – continued from previous page

ID	Position	Cloud	Dist. (pc)	$T_{\rm bol}$ (K)	$L_{\rm bol}$ ($L_\odot$)	$M_{\rm env}$[a] ($M_\odot$)	Region	Other names	Project[b]
33	04:21:11.4 +27:01:09.0	Tau	140	271	0.5	–		I04181+2654A	WILL (Tau02)
34	04:21:56.9 +15:29:45.9	Tau	140	24	0.1	–		IRAM 04191+1522	DIGIT
35	04:22:00.6 +26:57:32.0	Tau	140	178	0.4	–		FS Tau B	WILL (Tau03)
36	04:27:02.6 +26:05:30.0	Tau	140	159	1.4	0.6		DG Tau B	WILL (Tau04)
37	04:27:57.3 +26:19:18.0	Tau	140	52	0.5	0.1		I04248+2612 AB	WILL (Tau06)
38	04:29:30.0 +24:39:55.0	Tau	140	132	0.6	–		I04264+2433	WILL (Tau07)
39	04:31:34.1 +18:08:04.9	Tau	140	97	28	2.3		L1551 IRS5	DIGIT
40	04:35:35.3 +24:08:19.0	Tau	140	72	1.1	0.1		I04325+2402 A	WILL (Tau09)
41	04:39:53.9 +26:03:09.8	Tau	140	36	2.0	0.9		L1527, I04368+2557	DIGIT/WISH
42	04:39:13.9 +25:53:20.6	Tau	140	144	3.7	0.2		TMR 1, I04361+2547 AB	DIGIT/WISH
43	04:39:35.0 +25:41:45.5	Tau	140	172	2.2	0.2		TMC 1A, I04365+2535	DIGIT/WISH
44	04:41:12.7 +25:46:35.9	Tau	140	139	0.7	0.2		TMC 1, I04381+2540	DIGIT/WISH
45	08:25:43.9 -51:00:36.0	Core	450	104	27.9	4.4		HH 46	WISH
46	11:06:47.0 -77:22:32.4	Cha	178	56	0.8	0.2	Cham I	Ced110 IRS4	WISH
47	11:09:28.51 -76:33:28.4	Cha	178	–	2.9	–	Cham I	ISO192, CaINa2	WILL (Cha01)
48	12:01:36.3 -65:08:53.0	Core	178	84	7.1	2.7		BHR71	DIGIT/WISH
49	12:53:17.23 -77:07:10.7	Cha	178	550	38.0	0.8	Cham II	DK Cha, I12496-7650	DIGIT
50	12:59:06.58 -77:07:39.9	Cha	178	220	1.9	–	Cham II	ISO-CHAII 28	WILL (Cha02)
51	15:43:01.29 -34:09:15.4	Lup	130	52	1.6	0.5		I15398-3359	WISH
52	16:26:21.48 -24:23:04.2	Oph	125	254	4.4	0.1	L1688	Oph-emb 8, GSS30 IRS1, Elias 21	DIGIT
53	16:26:25.80 -24:24:28.8	Oph	125	35	1.0	0.8	L1688	Oph-emb 3, VLA 1623	DIGIT
54	16:26:44.2 -24:34:48.4	Oph	125	440	2.6	0.05	L1688	WL 12	DIGIT
55	16:26:59.1 -24:35:03.3	Oph	125	150	2.7	0.2	L1688	WL 22, ISO-Oph 90	WILL (Oph01)
56	16:27:09.36 -24:37:18.4	Oph	125	383	4.8	0.04	L1688	Oph-emb 16, Elias 29, WL 15	DIGIT
57	16:27:28.1 -24:39:33.4	Oph	125	633	0.8	0.3	L1688	Oph-emb 13, IRS 44	DIGIT
58	16:27:29.4 -24:39:16.1	Oph	125	633	0.8	0.3	L1688	IRS46	DIGIT
59	16:31:35.76 -24:01:29.2	Oph	125	580	1.6	0.3	L1709	Oph-emb 17, IRS 63	DIGIT
60	16:32:00.96 -24:56:42.7	Oph	125	150	7.7	0.1	L1689	Oph-emb 10	WILL (Oph02)
61	16:34:29.3 -15:47:01.4	Core	125	340	2.6	0.5		RNO 91	WISH
62	16:46:58.27 -09:35:19.8	Sco	125	–	1.0	0.1		L260 SMM1	WILL (Sco01)
63	18:17:29.9 -04:39:39.5	Core	200	49	10.2	4.4		L 483 MM	WISH
64	18:29:03.82 -01:39:01.5	Aqu	260	26	1.0	1.1		Aqu-MM2	WILL (Aqu01)
65	18:29:08.60 -01:30:42.8	Aqu	260	32	2.8	0.8		Aqu-MM4	WILL (Aqu02)

Continued on next page

Table 5.1 – continued from previous page

ID	Position	Cloud	Dist. (pc)	$T_{\rm bol}$ (K)	$L_{\rm bol}$ ($L_\odot$)	$M_{\rm env}{}^{a}$ ($M_\odot$)	Region	Other names	Project^{b}
66	18:29:49.56 +01:15:21.9	Ser	429	39	30.4	16.1		Ser-emb 6, Ser SMM1, FIRS1	WISH
67	18:29:56.7 +01:13:17.2	Ser	429	26	1.9	2.1		Ser SMM4	DIGIT/WISH
68	18:29:59.3 +01:14:01.7	Ser	429	38	5.1	3.2		Ser SMM3	DIGIT/WISH
69	18:29:37.70 -01:50:57.8	SerS	260	22	1.1	0.4		SerpS-MM1	WILL (SerS01)
70	18:30:04.13 -02:03:02.1	SerS	260	35	15	3.0		SerpS-MM18	WILL (SerS02)
71	18:30:25.10 -01:54:13.4	Aqu	260	217	1.0	0.3		Aqu-MM6	WILL (Aqu03)
72	18:30:28.63 -01:56:47.7	Aqu	260	306	1.6	0.4		Aqu-MM7	WILL (Aqu04)
73	18:30:29.03 -01:56:05.4	Aqu	260	34	0.6	0.2		Aqu-MM8	WILL (Aqu05)
74	18:30:49.94 -01:56:06.1	Aqu	260	43	0.8	0.2		Aqu-MM14	WILL (Aqu06)
75	18:31:09.42 -02:06:24.5	W40	260	37	4.2	0.7		W40-MM3	WILL (W40-1)
76	18:31:10.36 -02:03:50.4	W40	260	33	5.2	0.8		W40-MM5	WILL (W40-2)
77	18:31:46.54 -02:04:22.5	W40	260	26	8.1	1.2		W40-MM26	WILL (W40-3)
78	18:31:46.78 -02:02:19.9	W40	260	31	5.3	0.6		W40-MM27	WILL (W40-4)
79	18:31:47.90 -02:01:37.2	W40	260	25	6.6	0.7		W40-MM28	WILL (W40-5)
80	18:31:57.24 -02:00:27.7	W40	260	25	0.5	0.1		W40-MM34	WILL (W40-6)
81	18:32:13.36 -01:57:29.6	W40	260	33	0.5	0.1		W40-MM36	WILL (W40-7)
82	19:01:48.03 -35:57:22.2	CrA	130	209	1.7	2.0		RCrA IRS 5A	DIGIT
83	19:01:48.47 -36:57:14.9	CrA	130	63	0.7	–		RCrA IRS 5N	DIGIT
84	19:01:55.33 -36:57:17.0	CrA	130	79	9.1	–		RCrA IRS 7A + SMM 1C	DIGIT
85	19:01:56.42 -36:57:28.3	CrA	130	89	4.6	–		RCrA IRS 7B	DIGIT
86	19:02:58.67 -37:07:35.9	CrA	130	–	0.9	0.7		CrA-44, IRAS 32c	WILL (CrA01)
87	19:17:53.7 +19:12:20.0	Core	300	39	3.6	1.3		L 723 MM	WISH
88	19:37:00.9 +07:34:09.6	Core	106	37	0.5	1.2		B335	DIGIT
89	20:39:06.3 +68:02:16.0	Core	325	42	6.0	1.5		L1157	DIGIT
90	21:24:07.5 +49:59:09.0	Core	200	64	0.2	–		L1014	DIGIT

Notes. Numbered Per-emb and Oph-emb names come from Enoch et al. (2009), the Perseus / YSO names come from Jørgensen et al. (2006) and were subsequently used in Davis et al. (2008). Aqu, SerpS, and W40 numbered names are from Maury et al. (2011). Other source identifiers were compiled using Jørgensen et al. (2007b), Rebull et al. (2007), Davis et al. (2008), and Velusamy et al. (2013) (for Perseus), and Rebull et al. (2010) for Taurus. Chamaeleon names come from Spezzi et al. 2013 (Cham II) and Winston et al. 2012 (Cham I). $^{(a)}$ Envelope masses are from Kristensen et al. (2012) for WISH / DIGIT and Mottram et al. (in prep.) for WILL sources. $^{(b)}$ Source names used in the WILL program and entered in the Herschel Archive are written in brackets.

5.2.2 Observations and data reduction

Single footprint spectral maps of all our sources were obtained with the PACS instrument onboard *Herschel*. Each map consists of 25 spatial pixels (*spaxels*) of $9\farcs4 \times 9\farcs4$ arranged in the 5×5 array with a total field of view of $\sim 47'' \times 47''$. Each spaxel contains a (sub-)spectrum observed in first (red) or second (blue) order, within the wavelength ranges of 102-210 μm and 51-105 μm, respectively. The spectral resolving power increases with wavelength from about 1000 to 2000 (corresponding to velocity resolutions of ~140 to 320 km s^{-1}) in the first order and from about 1500 to 3000 (~100 to 210 km s^{-1}) in the second order.

Two main observing schemes were used: line spectroscopy mode for the WISH and WILL sources and range spectroscopy mode for the DIGIT sources. The line spectroscopy mode allows observations of small spectral regions ($\Delta\lambda$ ~0.5-2 μm) around selected lines and is particularly suited for deep integrations. The range spectroscopy mode provides the full spectrum from $\sim$ 50 to 210 μm but the spectral sampling within a resolution element is about 3-4 times coarser than in the line spectroscopy mode. For both schemes, the chopping / nodding observing mode within $6'$ from the source was used to subtract the background emission.

Data reduction for both observing modes was performed with the Herschel Interactive Processing Environment (HIPE, Ott 2010). The flux was normalized to the telescopic background and calibrated using observations of Neptune. Spectral flatfielding within HIPE was used to increase the signal-to-noise ratio (for details, see Herczeg et al. 2012 Green et al. 2013). Overall flux uncertainty is about 20% from cross-comparisons of sources in common within our programs.

The 1D spectrum is obtained by summing a custom number of spaxels chosen after investigation of the 2D spectral maps (Karska et al. 2013). For sources with extended line emission, the co-addition of spaxels with detected emission increases the S / N, smooths the continuum, and enables correction for significant differences in beam sizes over the wide spectral range covered by PACS. For sources with the point-like emission in all lines, only the central spaxel spectrum is used, but the line fluxes are multiplied by the wavelength-dependent instrumental correction factors ($\sim$ 1.4 at 70 μm and $\sim$ 2.3 at 180 μm, see PACS Observer's Manual[2]).

Since lines are spectrally unresolved (except [O I], see below), the line fluxes are calculated by fitting Gaussians to the final 1D spectrum. Single Gaussians are used for well-isolated lines and double or triple Gaussians for closeby lines, including blends. The line width of the Gaussians is fixed to the instrumental value of unresolved lines, except the [O I] line at 63 μm which often shows high-velocity wings (van Kempen et al. 2010b, Karska et al. 2013). In this case, integration and / or broad Gaussian fitting are applied.

---

[2] http://herschel.esac.esa.int/Docs/PACS/html/pacs_om.html

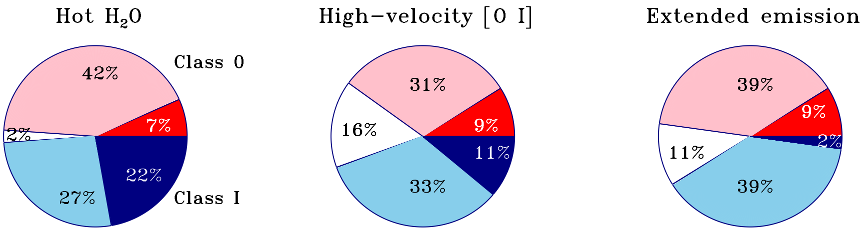

Figure 5.1 – Detection statistics for the hot H_2O 8_{18}-7_{07} line at 63 μm, high-velocity [O I] emission, and an extended pattern of line emission. Detections are shown in red (Class 0) and navy blue (Class I), non-detections for Class 0 sources are shown in pink and for Class I sources in light blue. The sources without $T_{\rm bol}$ determination (unknown Class) and contamination from nearby outflows and / or large-scale cloud emission in the [O I] line are shown in white.

5.3 Results

5.3.1 Detection statistics

PACS spectra of low-mass protostars show exclusively lines of CO, H_2O, OH, [O I], and [C II]. CO, H_2O and OH lines are seen in emission, with the exception of the H_2O 2_{12}-1_{01} line seen in absorption in a few fields with multiple outflows. The [O I] lines are seen in emission in the majority of cases, unless originating from large-scale photodissociation regions contaminating the off-position. The [C II] line at 158 μm is even more sensitive to the cloud emission and typically detected in the off-positions as well. In total, the CO 16-15 line targeted in the WISH, DIGIT, and WILL programs, is detected in 70 out of 90 sources, the H_2O 2_{12}-1_{01} line in 57 sources, and the OH doublet $^2\Pi_{3/2}$ $J = 7/2 - 5/2$ at 84 μm in 62 sources. Atomic emission associated with a YSO is detected in 71 sources in the [O I] 63 μm line and in 10 sources in the [C II] line.

Our large sample of sources also allows investigation of the detection statistics of interesting features found in PACS maps by previous studies. Figure 5.1 illustrates the percent of sources with the detections of hot H_2O, high-velocity [O I] emission, and an extended pattern of line emission.

A strong detection of the H_2O 6_{16}-5_{05} line at 63 μm ($E_{\rm up}$ ~ 1000 K) in the Class 0 protostar NGC1333 IRAS 4B was one of the first surprises revealed in the high-sensitivity *Herschel* / PACS data (Herczeg et al. 2012). The line flux of this H_2O transition in IRAS 4B exceeds the flux of the nearby [O I] line. Even though no other source in our sample shows such a bright H_2O 8_{18}-7_{07} line as found in IRAS 4B, the line is detected in about a quarter of our sources. The detections are non-evenly distributed for Class 0 and Class I sources – almost half of the Class I sources show the detection of the H_2O 8_{18}-7_{07} line in contrast to mere 14% of Class 0 sources. The line is also detected in Class II sources: in 4 out of 8 T Tauri stars in Fedele et al. (2013) and in 8 out of 33 gas-rich T Tauri disks (or 68 in total) in Riviere-Marichalar et al. (2012). Interestingly, the H_2O 8_{18}-7_{07} line is often detected in the absence of lower−J H_2O lines for those more evolved sources and most likely originates from the disk (Fedele et al. 2012, 2013, Riviere-Marichalar et al. 2012).

PACS spectral maps of the [O I] and [C II] lines at 63 and 158 μm provide a means to disentangle the emission associated with a young protostar from the large-scale cloud emission and to fully explore the diagnostic potential of these forbidden lines. [C II] emission is very rarely associated with YSOs and primarily traces the photodissociated regions of molecular clouds (Karska et al. 2013). Since the [C II] emission is typically detected at the off-positions and subtracted by chopping, most of the maps show more or less uniformly distributed [C II] in absorption. Only 10 sources show [C II] in emission, related either to the central or outflow positions of YSOs.

Unlike maps in the [C II] line, the majority of our sources show [O I] emission related to YSOs with the pattern strongly indicating an origin in the jet / outflow (Green et al. 2013, Karska et al. 2013). The spectral resolution of PACS is about 90 km s^{-1} at these wavelengths, resolving only the highest-velocity, jet-related component of the [O I] line. The [O I] velocity shift is most clearly seen in the red outflow of HH 46 (van Kempen et al. 2010b), while for the other sources the best signature of high-velocity emission is a broad line width, exceeding the best-fit Gaussian profile reproducing the maximum intensity. In total, 20% of sources, evenly distributed among Class 0 and I sources, show high-velocity emission associated with the [O I] line.

Spatially-extended emission in molecular lines is not as common a feature as seen in the [O I] line. The H_2O 2_{12}-1_{01} line at 179 μm is clearly extended in several well-known Class 0 outflow sources, most notably in the cases of L1157 (Nisini et al. 2010a), L1448 (Nisini et al. 2013), and NGC1333 IRAS 4A (Karska et al. 2013, Santangelo et al. 2014). The statistical study of the line emission extent is only possible based on the single footprint 5×5 maps. Preliminary analysis showed significant variation, with almost half of the sources in the WISH sample having extended emission (Karska et al. 2013), but only a minor fraction in the DIGIT sample (Green et al. 2013). Extended molecular emission is only detected in 8 Class 0 and 2 Class I sources in our combined sample beyond the central 9.4″ spaxel, altogether only ∼ 10% of 90 sources. The large fraction of sources with extended emission in the WISH sample is due to the observational bias in the source sample, where sources with strong outflow emission were preferentially selected.

5.3.2 Cross-species line flux correlations

Correlations between line fluxes are a useful indicator of which groups of species are related to the same and / or different physical components in a YSO. Karska et al. (2013) found strong line flux correlations between H_2O and high$-J$ CO lines and, based also on the similarity in their spatial distribution, suggested a common origin in non-dissociative shocks. A lack of correlation was found with the [O I] line, which traces dissociative shocks and to a smaller extent the hidden atomic jet (Karska et al. 2013). Weak correlations of OH with H_2O and its similar spatial distribution to that of [O I] indicated that OH is also partly tracing the dissociative shocks.

Figure 5.2 revisits the above results using an extended sample of sources and most-commonly detected lines of CO, H_2O, OH, and [O I] observed in the WISH, DIGIT, and WILL programs. The correlations are quantified following the formulation of a correlation factor, r, in Marseille et al. (2010, Appendix A), that can be translated to the significance

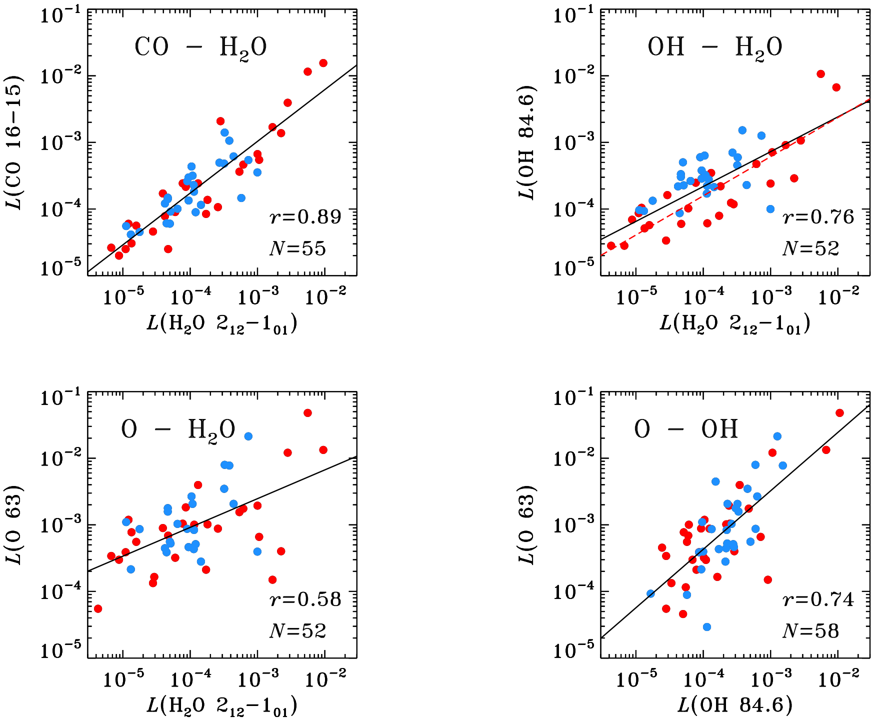

Figure 5.2 – Flux correlations between the H_2O 2_{12}-1_{01} line at 179 μm and the CO 16-15 and OH 84.6 μm lines (top) and the [O I] 63 μm line with the H_2O 2_{12}-1_{01} and OH 84.6 μm lines (bottom). Class 0 sources are shown in red and Class I sources in blue. Solid lines show the best linear fits obtained with a least-squares method. A separate fit to the Class 0 sources only is shown on the H_2O - OH plot as red dashed line. Correlation coefficients (r) and number of sources with line detections (N) are shown on the plots.

level of a correlation when multiplied by $\sqrt{N-1}$, where N is the sample size. Using this procedure, the strongest, 6.5σ correlation is found between the H_2O and CO lines and a somewhat weaker, 5.4σ correlation is seen between the H_2O and OH lines. The weakest, 4.1σ correlation is obtained between the H_2O and [O I] lines, while the [O I] and OH lines correlate at the 5.6σ level.

While these results are qualitatively consistent with the results from the WISH sample, the extended sample allows a further distinction between the Class 0 and I sources. The H_2O – CO line fluxes are correlated at a significance of 4.8σ for Class 0 sources and 4.0σ for the Class I sources. The H_2O and OH lines show correlations of 4.4σ for Class 0 sources and only 2.6σ for Class I sources.

Clearly, the correlations between the pairs of molecular lines are stronger for the less evolved Class 0 sources, while a comparable, 4σ correlation is found between the [O I] and OH line fluxes for both Class 0 and I sources. At the same time, the OH line luminosities are larger for the Class I sources with the same H_2O fluxes as the Class 0 sources (see the H_2O – OH panel), suggesting that the fraction of OH associated with the component traced by the [O I] line increases for more evolved sources.

The different origin of H_2O and [O I] emission, revealed by the weak correlation between the two species, is further supported by differences in the correlations with source physical parameters (see Figures 5.B.1 and 5.B.2 Appendix B). The [O I] line is tightly related to the source bolometric luminosity, $L_{\rm bol}$, while the H_2O line luminosities are mostly influenced by the envelope mass, $M_{\rm env}$. The trend for H_2O could be a pure excitation effect, since the lines are subthermally excited. However, a recent study of spectrally resolved HIFI line profiles of the same sources shows a decreasing line width of the H_2O lines from Class 0 to Class I (Mottram et al. submitted), showing that evolution also influences the H_2O - $M_{\rm env}$ relation.

5.4 Analysis

5.4.1 CO excitation

Rotational temperatures ($T_{\rm rot}$) and number of molecules ($\mathcal{N}$) of the emitting gas from low-mass YSOs are routinely calculated from PACS spectra using Boltzmann diagrams (e.g. Green et al. 2013, Karska et al. 2013, Manoj et al. 2013). The most meaningful results are obtained for CO, since its excitation is dominated by collisions and the lines are mostly optically thin (based on the upper limits on ^{13}CO line fluxes, Goicoechea et al. 2012, Lee et al. 2013). The CO rotational diagrams in the PACS range covering J =14-13 up to 49-48 show a break around the $J = 24 - 23$ transition and therefore are often fitted with two straight lines. The corresponding components are referred as the 'warm' and 'hot' (Karska et al. 2013), to distinguish them from the 'cold', 70-100 K component detected at $J \lesssim 10$ transitions (Goicoechea et al. 2012, Yıldız et al. 2013). Rotational temperatures obtained in this manner are surprisingly similar in all low-mass embedded YSOs, and equal to about 300-350 K (CO $J \sim 14 - 24$ lines) and $\gtrsim 700$ K (CO $J \gtrsim 24$ lines), respectively. Similar values of the warm component temperatures are even seen in much more massive protostars (Karska et al. 2014), further suggesting that an underlying universal physical mechanism is responsible for the excitation in all sources. The number of emitting molecules varies more strongly from source to source, increasing with source bolometric luminosity (Figure 25 of Green et al. 2013, see also Manoj et al. 2013).

In the following sections, rotational temperatures and number of emitting molecules are correlated with source physical parameters (bolometric luminosities and envelope masses) and compared on a cloud-to-cloud basis. The CO diagrams for the WISH sources are presented in Karska et al. (2013) and for the DIGIT sources in Green et al. (2013), Lee et al. (2013), Dionatos et al. (2013), Lindberg et al. (2014), and J.-E. Lee et al. (submitted). The procedures used to derive meaningful parameters from rotational diagrams with a limited number of targeted lines and associated errors are explained in Appendix B, where the remaining diagrams for the WILL sources are also shown (Figures 5.C.1 and 5.C.2).

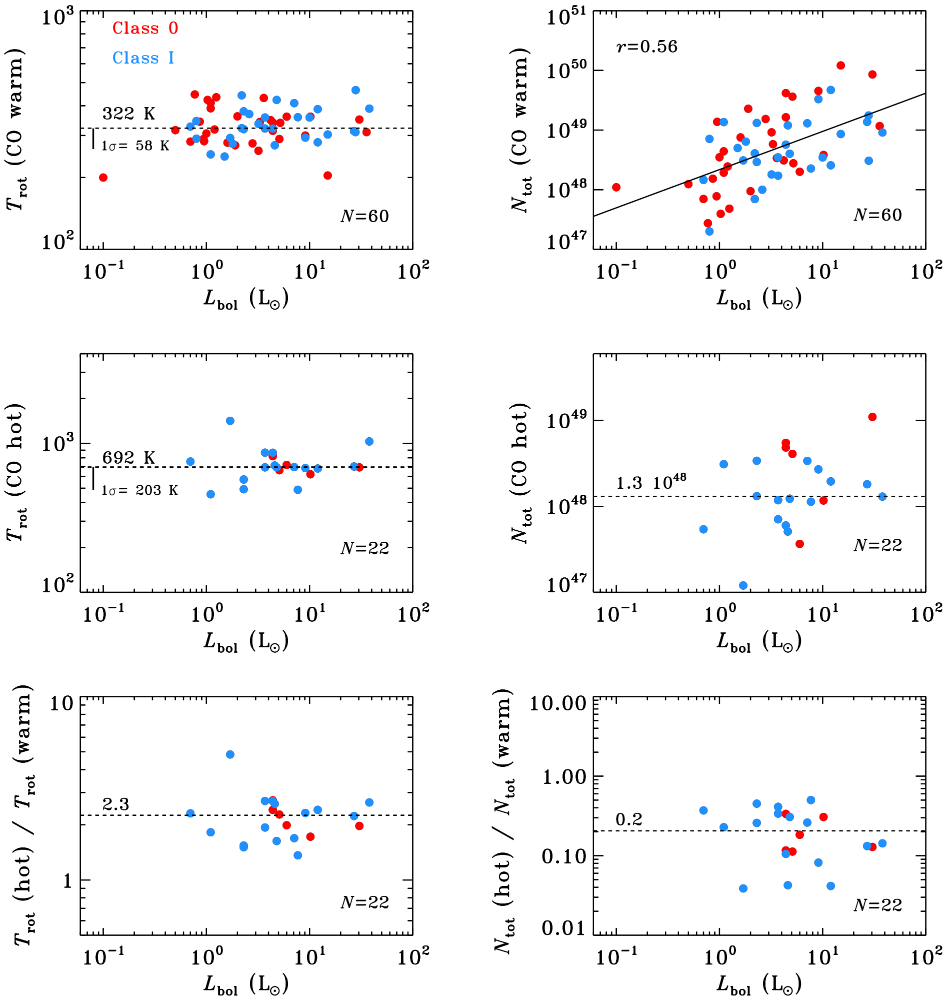

Figure 5.1 – CO rotational temperatures (left) and numbers of emitting molecules (right) for the 'warm component' (top), 'hot component' (middle), and their ratios in the 'hot' and 'warm' components as a function of bolometric luminosity. Solid lines show the best linear fits obtained with a least-squares method, only for the cases where the correlation coefficient r exceeds the 2σ threshold (see text). Otherwise, the median values are shown in dashed lines. Class 0 sources are shown in red and Class I sources in blue.

5.4.1.1 Correlations with source physical parameters

The left panel of Figure 5.1 shows the rotational temperatures of CO in the warm and hot components, and the ratio of the temperatures in the two components, as functions

Table 5.1 – Correlation coefficients for CO excitation and sources parameters relations

	$L_{\rm bol}$		$M_{\rm env}$	
	r	N	r	N
$T_{\rm rot}$ (warm)	0.17	60	-0.27	48
$T_{\rm rot}$ (hot)	0.09	22	0.06	20
$T_{\rm rot}$ (hot) / $T_{\rm rot}$ (warm)	-0.06	22	0.20	20
$\mathcal{N}$ (warm)	**0.56**	60	**0.65**	48
$\mathcal{N}$ (hot)	0.33	22	**0.79**^{a}	18^a
$\mathcal{N}$ (hot) / $\mathcal{N}$ (warm)	-0.24	22	-0.43	20

Notes. Correlation coefficients exceeding the 3σ threshold values are shown in boldface. Positive coefficients are indicators of correlations while negative – the anti-correlations. No correlations are found with bolometric temperature, $T_{\rm bol}$. $^{(a)}$ R CrA IRS 5A and L1157 are excluded from the fit. The correlation coefficient when the two sources are included is 0.47, below the threshold.

of source bolometric luminosity. The warm component in the CO diagrams is detected in 60 sources with a median rotational temperature of ~320 K and standard deviation of ~60 K. The hot component is seen in only 22 sources with a corresponding median temperature of ~690 K and standard deviation of 200 K. The larger spread in the hot component temperatures is most likely due to the fewer lines detected in this component and their lower S/N; the intrinsic spread may be smaller. The ratio of the hot and warm rotational temperatures is of order 2.

The correlation coefficients between rotational temperatures or their ratio and source bolometric luminosities (Table 5.1) are in all cases below the 3σ threshold value, equal to $r_{\rm t} = 0.39$ for $N = 60$ sources and 0.65 for $N = 22$ sources (Marseille et al. 2010). Therefore, in line with previous studies, CO rotational temperatures are not related to the source bolometric luminosities even in this much larger source sample.

On the other hand, the coefficient of $r = 0.56$, translating to the 4.3σ significance level, strongly suggests a correlation between the number of emitting warm CO molecules and the bolometric luminosity (right panel of Figure 5.1). No such correlation is found for the hot component numbers of molecules and their ratio with the number of warm molecules, likely due to the less accurate measurements and limited source sample with a detected hot component. The median of the number of molecules in the hot component is $1.3\ 10^{48}$ molecules, while the ratio of the hot over warm number of molecules is about 0.2.

Similar results are obtained when the CO rotational temperatures and emitting molecules are correlated with the envelope masses (Figure 5.2). Small differences between the median values are due to a somewhat lower number of sources with known envelope masses. Note, however, that the correlations between numbers of emitting molecules and the envelope masses are **stronger** than those with bolometric luminosities (Table 5.1). In particular, the number of molecules in the warm component correlates with a higher, 5σ confidence level. Moreover, an additional correlation is found between the hot component and envelope mass. The strength of this correlations is at the 2σ correlation threshold when all 20 sources are considered, but increases to the 3.7σ level when the two outlying sources

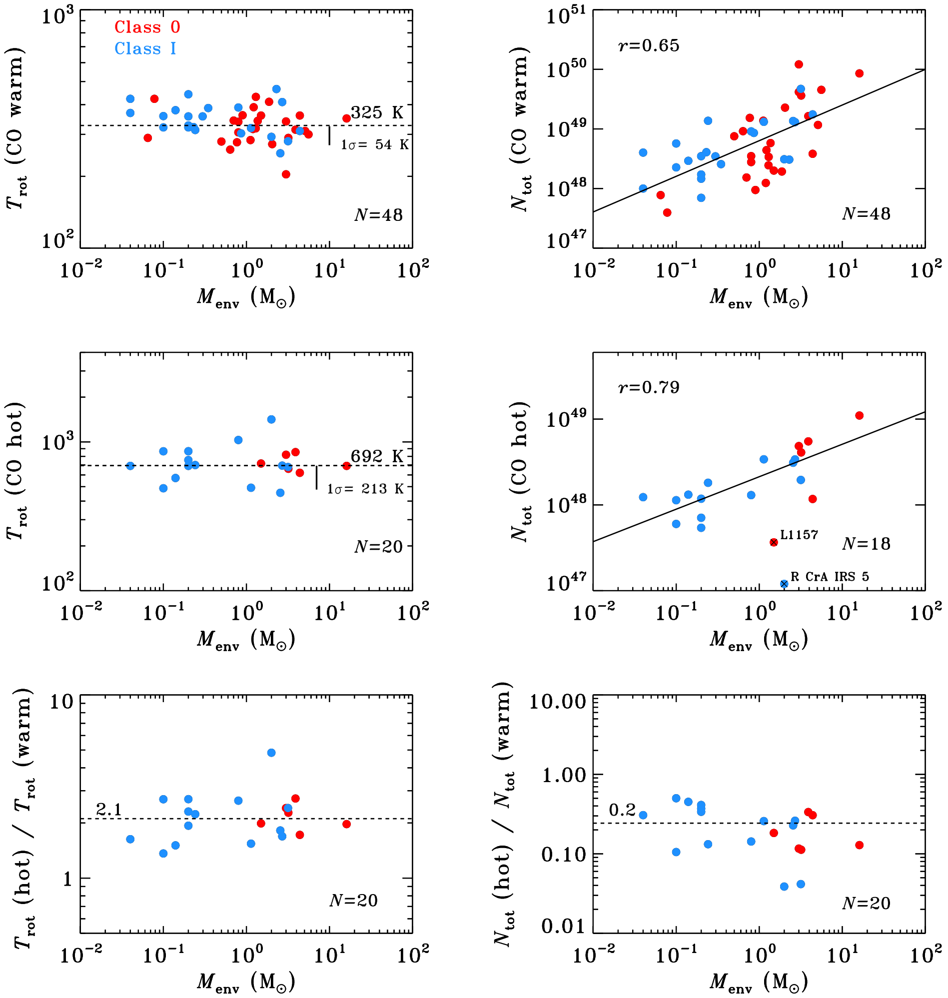

Figure 5.2 – Similar to Figure 5.1, except that all the quantities are shown as a function of envelope mass. Class 0 source L1157 and Class I source R CrA IRS 5A are not taken into account for the fit in the total number of hot molecules versus envelope mass plot (see text) and overplotted with a black cross.

are excluded. These outliers are the Class 0 source L1157 and Class I source R CrA IRS 5A.

Table 5.2 – CO excitation in selected molecular clouds

Cloud	CO warm component			CO hot component			Ratio[a]
	N (% obs)	$T_{\rm rot}$ (K)	$\mathcal{N}_{\rm w}$ (10^{48})	N (% obs)	$T_{\rm rot}$ (K)	$\mathcal{N}_{\rm h}$ (10^{48})	
Per	23 (77 %)	318	6.4	7 (23 %)	678	3.1	0.23
Tau	10 (71 %)	359	1.0	3 (21 %)	755	0.7	0.37
Oph	7 (78 %)	345	3.5	3 (33 %)	690	1.1	0.31
Aqu	2 (33 %)	281	14.5	0 (0 %)	–	–	–
W40	1 (14 %)	339	2.8	0 (0 %)	–	–	–
CrA	5 (100 %)	293	3.1	3 (60 %)	710	0.5	0.04
All	60 (67 %)	322	3.9	23 (26 %)	690	1.3	0.21

Notes. The bottom line refers to all sources and not only the ones from the clouds mentioned specifically in the table.
([a]) The ratio of numbers of emitting CO molecules in the hot and warm components.

5.4.1.2 Cloud-to-cloud differences

Median rotational temperatures and numbers of emitting molecules are calculated separately for YSOs in different molecular clouds in Table 5.2. The warm component in the CO diagrams is most commonly detected in YSOs located in Corona Australis (all sources), Ophiuchus, Perseus, and Taurus (~70-80 %), and much less frequently detected for sources in the W40 and Aquila molecular clouds (15-30 % detection rate). Similarly, the hot component is detected most often in Corona Australis sources (60 %), less often in Ophiuchus (30 %), Perseus and Taurus (~20 %), and never detected in W40 and Aquarius.

As expected from the previous section, the spread in rotational temperatures between sources in different clouds is small. More significant differences are seen in the total numbers of emitting CO molecules. $\mathcal{N}_{\rm w}$ is the largest in the Aquila (~15 10^{48}) and Perseus sources (~6 10^{48}), and smallest in the Taurus sources (~1 10^{48}), and of order of ~3 10^{48} for the remaining YSOs. The large number of emitting molecules in the warm component does not directly translate to detections of the hot component, as seen in the Aquila sources. Typically, $\mathcal{N}_{\rm h}$ is of order of 1 10^{48} for all sources. The ratio of the hot-to-warm numbers of molecules is the lowest for Corona Australis sources (~0.04), and up to an order of magnitude larger, 0.2-0.4, for the remaining clouds.

Environment is therefore not a critical factor for the CO excitation. The differences between YSOs in Perseus and Taurus are not significant, and for the rest of the clouds the samples are too small for definitive conclusions. The CO non-detections in Aquila and W40 are more likely due to low-luminosities of the protostars and not intrinsic cloud differences.

5.4.2 Molecular and atomic cooling

Previous FIR surveys have shown that the proportion of atomic to molecular emission in low-mass protostars changes as they evolve (Nisini et al. 2002b, Podio et al. 2012, Karska et al. 2013). We revisit these results using our larger sample of sources which is more evenly distributed over the Class 0 and I stages.

The total luminosity in the atomic lines is calculated by summing the fluxes of the two [O I] lines in the PACS spectra, at 63 and 145 μm. For the WILL sources where only the 63 μm line was targeted, the median ratio of the two oxygen lines from the WISH survey ([O I] 63 / [O I] 145 = 10.5, Karska et al. 2013) is used to correct for the missing flux of the [O I] 145 μm line. The [C II] line flux is not included in the atomic luminosities because it is either non-detected or contaminated by the larger-scale cloud emission for the majority of our sources. Unlike the surveys of Giannini et al. (2001) and Nisini et al. (2002b) using the single ISO beam of 80′′, only objects with [O I] emission spatially associated with the studied sources are included in our analysis. As demonstrated in Table E.1. of Karska et al. (2013), PACS fluxes are up to a factor of a few lower than the ISO values for the same sources, most probably due to elimination of the cloud contribution to the [O I] emission.

The total far-infrared (55-210 μm) luminosity of the CO lines is calculated for our sources in two ways. For sources with full PACS spectra (from the DIGIT program), the total flux in the CO lines is simply the sum of fluxes from all detected lines. For sources for which only selected CO transitions were targeted (from the WISH and WILL programs), the CO rotational temperatures were used to obtain the fluxes of the missing lines. The procedure is applied only for sources with a minimum of three detected lines in each of the (warm and / or hot) components on the CO diagrams. In particular, for cases where the hot component temperature could not be well-determined, the warm component temperature is used for extrapolation. The extrapolation to lower$-J$ transitions not accessible to PACS ($J_u < 14$) is not done due to the fact that the so-called ‘cold’ component on CO diagrams traces the entrained outflow gas of $T \lesssim 100$ K (Yıldız et al. 2013, Goicoechea et al. 2012), not the shocked, $T \gtrsim 300$ K gas seen by PACS.

The histograms of total CO and [O I] luminosities over bolometric luminosities ($L_{\rm CO}$ / $L_{\rm bol}$ and $L_{\rm [OI]}$ / $L_{\rm bol}$) and of the ratio of the cooling in the two species ($L_{\rm CO}$ / $L_{\rm [OI]}$) are presented in Figure 5.3. The histogram of $L_{\rm CO}$ / $L_{\rm bol}$ peaks in the 10^{-3}-$10^{-2.5}$ bin for Class 0 sources and in the $10^{-3.5}$-10^{-3} bin for Class I sources, demonstrating that the fractional CO luminosity decreases for the more evolved sources. This is also reflected by the observed ranges of $L_{\rm CO}$ / $L_{\rm bol}$, which extend to larger values for Class 0 sources and to smaller values for Class I sources.

Such a trend is not seen when histograms of $L_{\rm [OI]}$ / $L_{\rm bol}$ for the two classes of sources are compared. The ratio peaks in the 10^{-4}-10^{-3} bins with a small fraction of sources with higher or lower ratios up to an order of magnitude, irrespective of the evolutionary stage. These results are qualitatively different from previous studies with ISO, where the histogram for Class 0 sources peaked 2 orders of magnitude higher compared to the Class I sources, at about $10^{-2.5}$ (Nisini et al. 2002b, see also Podio et al. 2012). The large absolute values of $L_{\rm [OI]}$ / $L_{\rm bol}$ from ISO indicate significant contamination from nearby cloud emission, which could possibly be more severe in the surroundings of Class 0 sources.

The histograms of the $L_{\rm CO}$ / $L_{\rm [OI]}$ for Class 0 and I sources both peak in the 10^{0}-$10^{0.5}$ bin, showing that typically the CO luminosity is equal to or up to a factor ~ 3 larger than the [O I] luminosity. There is a tail of Class 0 sources with an even larger fraction of CO to [O I] luminosities. The histogram for the Class I sources is more symmetric, with only

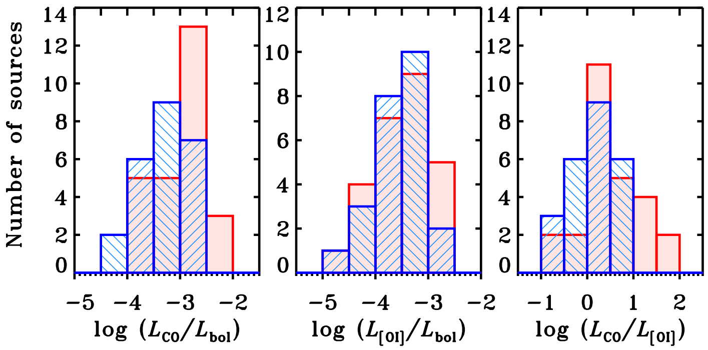

Figure 5.3 – Histograms of the CO (left) and [O I] (center) cooling over bolometric luminosity and the ratio of cooling in CO and [O I] (right). The red color shows the distributions for Class 0 sources and blue for Class I sources.

a slightly higher number of sources at lower L_{CO} / $L_{[OI]}$ ratios, corresponding to large fractions of atomic oxygen emission. In total, however, more sources in the Class I stage have more luminosity in CO than in atomic lines, but the maximum L_{CO} / $L_{[OI]}$ values are up to an order of magnitude lower than for the Class 0 sources. Similar trends have been reported in Nisini et al. (2002b) and Karska et al. (2013) for smaller samples of sources.

The large scatter in the rotational diagrams of H_2O and OH (Karska et al. 2013, Wampfler et al. 2013) implies that the accuracy of extrapolated fluxes of lines not targeted in the WISH and WILL programs is significantly lower than for the case of CO (Lee et al. submitted). Therefore, molecular cooling in H_2O and OH lines and, consequently, the total far-infrared cooling, can only be well-determined for a limited sample of sources with full PACS spectra observed in the DIGIT and WISH programs and is not presented here.

5.4.3 Mass flux rates in jets and outflows

Maps of outflows in low−J CO lines are commonly used to calculate outflow energetics of the entrained material in low-mass young stellar objects (e.g. Curtis et al. 2010, van der Marel et al. 2013, Yildiz et al. subm.). The outflow mass can be derived from the total column density of CO by conversion to H_2 mass over the whole area of the outflow (details in Appendix C in van der Marel et al. 2013). The mass outflow rate is then calculated by dividing the mass by the so-called ‘dynamical age’ of the outflow, which is obtained

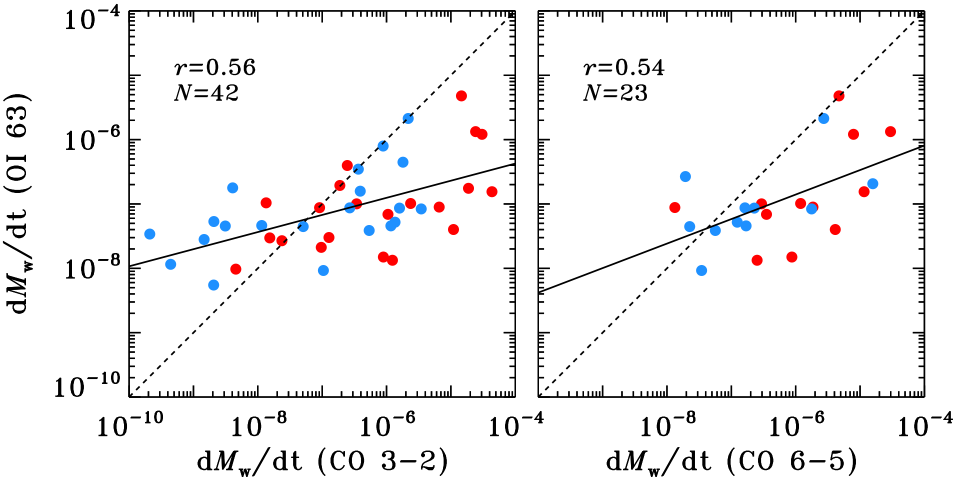

Figure 5.4 – Wind mass flux rates calculated from the [O I] line and CO 3-2 (left, from Mottram et al. in prep) and CO 6-5 (right, from Yildiz et al. subm.) lines. Solid lines show the best fit to the data and the dashed lines show the y = x function.

from the current outflow extent and the maximum velocity seen in the CO line wings. Therefore, the CO mass flux rate is by definition an 'integrated' mass flux rate over the outflow lifetime and is sensitive to the assumed outflow inclination. If momentum flux conservation applies, the wind mass flux rate implied by the CO lines, $\mathrm{d}M_{\mathrm{w}}(\mathrm{CO})/\mathrm{dt}$, is subsequently calculated by multiplying the observed CO rate by the ratio of maximum velocity of CO line profiles and the assumed wind velocity of 100 km s^{-1}.

An alternative method of calculating the mass flux rates was proposed by Hollenbach (1985), who showed that for the range of physical conditions found in YSOs the mass flux rates scale with the [O I] line luminosity, $\mathrm{d}M_{\mathrm{w}}/\mathrm{dt}=10\ L(\mathrm{O\,I}\ 63)$, in units of 10^{-5} $\mathrm{M}_{\odot}$ yr^{-1}. The formula is valid under the assumption that the [O I] line traces primarily the dissociative shock caused by the impact of the jet / wind on the surrounding cloud. The contribution from the non-dissociative outflow shocks is assumed to be negligible and effects of outflow geometry are neglected.

Figure 5.4 and Table 5.3 compare the mass flux rates calculated using the two methods. The majority of the sources show higher mass flux rates inferred from the CO lines, with only a few sources lying on the y = x line. There are also about 10 sources with lower mass flux rates derived from CO 3-2 than [O I]. Those low CO / [O I] mass flux rates sources are typically Class I sources observed as part of the WILL program. Overall, the CO 3-2 and [O I] mass flux rates show a $\sim 3.6\sigma$ correlation with the slope clearly deviating from the y = x function.

The median [O I] mass flux rate equals about 5 10^{-8} $\mathrm{M}_{\odot}$ yr^{-1}, of the same order for both Class 0 and I sources (Table 5.3). The median CO 3-2 and CO 6-5 mass flux rates are of order 10^{-7}-10^{-6} $\mathrm{M}_{\odot}$ yr^{-1}, but those are obtained for a subsample of sources observed in [O I]. The median ratios of the CO 3-2 / [O I] and CO 6-5 / [O I] are of the order

Table 5.3 – Jet / outflow mass loss rates from [O I] and CO lines

	dM_w/dt ($M_\odot$ yr^{-1})			Ratios of dM_w/dt	
	[O I] 63 μm	CO 3-2	CO 6-5	CO 3-2 / [O I]	CO 6-5 / [O I]
All (median)	5.4 10^{-8}	1.2 10^{-7}	3.5 10^{-6}	3	4
(mean)	2.4 10^{-7}	3.3 10^{-6}	3.7 10^{-6}	27	19
Class 0	4.3 10^{-8}	1.2 10^{-7}	1.5 10^{-6}	5	15
	2.6 10^{-7}	3.0 10^{-6}	5.2 10^{-6}	47	27
Class I	7.0 10^{-8}	1.9 10^{-7}	1.6 10^{-7}	1	2
	2.1 10^{-7}	5.3 10^{-6}	1.9 10^{-6}	27	10

Notes. CO 3-2 mass loss rates are from Mottram et al. (in prep.) and Yildiz et al. (subm.), for WILL and WISH / DIGIT sources respectively. CO 6-5 rates are calculated for the same WISH / DIGIT sources in Yildiz et al. (subm.).

of unity for both Class 0 and I sources. Larger differences between the two methods of determining wind mass flux rates are seen when the mean values are compared (Table 5.3). In particular, the mean CO / [O I] ratios are of the order of 10, indicating that some of the sources with the largest wind mass flux rates inferred from CO are at the same time weak in [O I].

Note that the CO maps were obtained in a uniform way and the mass outflow rates were calculated using the same method with absolute uncertainties of a factor of a few (van der Marel et al. 2013). Lower rates from the CO 3-2 with respect to CO 6-5 maps (Table 5.3) are due to the intrinsic differences in the sample of sources: the CO 3-2 data are obtained for a significantly larger number of sources, including the low luminosity sources from the WILL program. Despite these differences, the results are qualitatively the same for the CO 3-2 and CO 6-5 rates, as seen in Figure 5.3. For more detailed discussion of these results see §5.5.3.

5.4.4 Comparisons to models of shocks and photodissociation regions

Since PACS does not resolve the emitting regions of the molecules and atoms, comparisons of such observations with shock models have concentrated on line ratios (e.g. Santangelo et al. 2012, Vasta et al. 2012, Lee et al. 2013, Santangelo et al. 2013, Karska et al. subm.). Various molecular ratios indicate an origin in $C-$type shocks, which emit copiously in CO, H_2O, and OH, but produce very little [O I] emission.

[O I] shock predictions are calculated using the Flower & Pineau des Forêts (2003) model for a finely-sampled grid of shock velocities υ, from 10 to about 50 km s^{-1}, and two pre-shock densities, $n_H = 10^4$ and 10^5 cm^{-3}. The model intensities in units of erg cm^{-2} s^{-1} sr^{-1} are translated to W cm^{-2} assuming that the emission entirely fills one spaxel in the PACS maps (1 sr $\sim$ 2.1 10^{-9} π). The one spaxel size is chosen despite the fact that PACS maps in the [O I] and [C II] lines often show emission extending to more than one spaxel (this work and Karska et al. 2013), because the actual emitting region observed

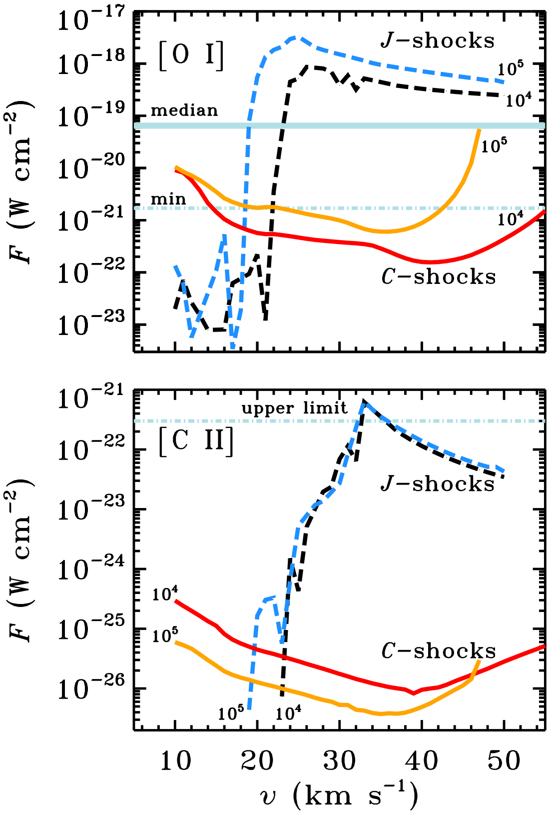

Figure 5.5 – Absolute fluxes of the [O I] line at 63 μm (top) and the [C II] line at 158 μm (bottom) predicted by *C*- and *J*-shock models of Flower & Pineau des Forêts (2003) and confronted with observations. Median observed fluxes of [O I] shown in the top panel are calculated only for those sources where the emission is associated with the source and not large-scale cloud emission. The minimum detected flux of [O I] is shown also for reference. In case of [C II], in the rare cases that the line is actually detected and spatially associated with the source, the fluxes exceed the range shown in the bottom panel. The instrumental upper limit for the line detection is shown as reference.

by each spaxel is likely only a fraction of the spaxel size (‘filling factor’ below unity). A possible underestimate of a factor of a few of the emitting region size does not affect the conclusions below given the orders of magnitude variations probed by the models and observations.

Comparison of absolute observed and model line fluxes of the [O I] 63 μm and [C II] 158 μm lines are shown in Figure 5.5 (top panel). The median observed [O I] flux, calculated for sources with emission spatially associated with YSOs, equals $\sim 10^{-19}$ W cm^{-2} and falls between the predictions for the *C*− and *J*−type shock models for a wide range of shock velocities. The *C*−type shock model fluxes decrease from about 10^{-20} W cm^{-2}

by 1 and 2 orders of magnitude in the velocity range from 10 to about 40 km s^{-1} for the assumed pre-shock densities of 10^5 cm^{-3} and 10^4 cm^{-3}, respectively. Above 40 km s^{-1}, the fluxes increase to values as high as to 10^{-19} W cm^{-2} for the models with higher pre-shock densities, but still not sufficient to explain the [O I] emission in many of the brightest sources. The $J-$type shock model fluxes, on the other hand, fit even the brightest observed [O I] lines. A sharp increase from about 10^{-22} W cm^{-2} to 10^{-18} W cm^{-2} occurs when the shock becomes dissociative at velocities of about 20 km s^{-1}. Depending on the size of the emitting region, likely lower than the full spaxel area, the observations of all absolute line fluxes of [O I] can be reproduced with $J-$type shocks.

The observed fluxes and limits of the [C II] line at 158 μm greatly exceed the model predictions for both $C-$ and $J-$type shock models (Figure 5.5, bottom panel). Whenever the line is detected and associated with a YSO, the fluxes exceed 10^{-21} W cm^{-2}, 4 orders of magnitude above the model $C-$ shock fluxes and a factor of a few above the peak [C II] flux from the $J-$ shocks, at about 30 km s^{-1}. In many sources, however, the [C II] line is not detected and only the upper limit can be used for comparisons with the models. For those sources, the observed limit is consistent with both $J-$ and $C-$type shocks.

Since the shock models cannot reproduce the observed [C II] fluxes for the sources where it is detected, [C II] is most likely the result of CO photodissociation and photoionization of C. This requires hard UV photons with $\lambda < 1100$ Å, likely produced in the vicinity of the protostar, in accretion flows in the star-disk boundary layer and / or fast bow-shock (e.g. Spaans et al. 1995, van Kempen et al. 2009a). Models of photodissociation regions (PDRs, Tielens & Hollenbach 1985) can be used to constrain the UV field and densities using absolute intensities of atomic and ionic lines as well as molecules. In our case, where most of the molecular emission and a part of [O I] emission originates from shocks, comparisons to absolute line intensities of [C II] are the most reliable measure of FUV alone. To better constrain the range of possible parameters, the ratio of [C II] and [O I] can be used, taking into account that a fraction of the [O I] emission comes from the dissociative shocks. This ratio rapidly decreases with density, controlled mainly by [O I] with its high critical density of about $\sim 5\ 10^5$ cm^{-3}, two orders of magnitude higher than for [C II] (Kaufman et al. 1999).

Figure 5.6 compares the observed [C II] / [O I] versus [C II] intensities and the PDR model predictions from Kaufman et al. (1999). The [C II] intensities are calculated assuming a size of one spaxel and shown only for sources where the [C II] emission is spatially associated with YSOs. The range of observed [C II] intensities equals 10^{-5}-10^{-4} erg cm^{-2} s^{-1} sr^{-1}, whereas [C II] / [O I] ranges from 10^{-2}-10^{0}. The corresponding model densities are in the range from 10^5 cm^{-3} to 10^6 cm^{-3}. The majority of the sources show a very similar incident UV field, about 10^2 G_0 on scales of ~1000 AU, with the exception of a more massive source – Serpens SMM1 (#66) – in the 10^3 G_0 regime.

Possible contributions from shocks to the [O I] intensity would decrease both the densities and the UV field matching the observations (see Figure 5.6). For example, if 90% of [O I] flux comes from the shock, corresponding to an increase of observed [C II] / [O I] by a factor of 10, the best fit densities are in the range 10^4-10^5 cm^{-3} and UV field of $\sim 10^1$-10^2 G_0.

Finally, we note that the diagnostic diagram from Figure 5.6 can be used to distinguish

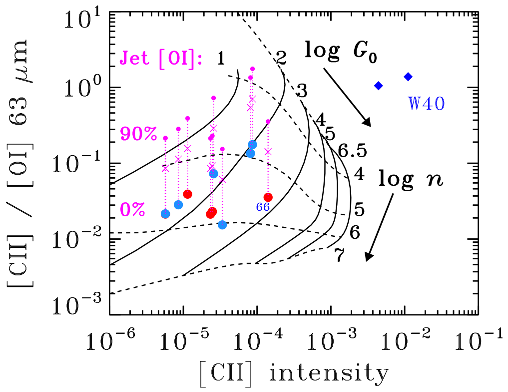

Figure 5.6 – Observed line ratio of the [C II] line at 158 μm and the [O I] line at 63 μm as function of the [C II] line intensity (red dots for Class 0 and blue dots for Class I objects) and models of photodissociation regions from Kaufman et al. (1999). Models are shown for densities from 10^3 to 10^7 cm^{-3} (in dashed lines) and for incident UV from 10^1 to $10^{6.5}$ G_0 (in solid lines). Small magenta dots and crosses indicate line ratios assuming that 90% and 75% of [O I] flux comes from the jet, respectively. Two cloud-related PDR regions in the W40 cloud are shown with blue diamonds.

between PDRs associated with YSOs and clouds. For comparison with the local PDRs, two sources observed within a strong PDR in the W40 cloud (W40-2 and W40-3) are shown. Both of them are located in the low-density and high-UV regime that is very distinct from our observed YSOs.

5.5 Discussion

As demonstrated in the previous sections, far-IR lines can inform about the physical processes in the surroundings of young protostars. First, the origin of the CO line emission is discussed based on excitation diagrams and correlations presented in §1.4.1. Second, possible scenarios responsible for the [O I] emission are considered, which are finally related to the mass loss rates calculated based on the [O I] luminosity.

5.5.1 Origin of CO emission: a two-shock scenario

Similar to individual and small subsample studies with *Herschel* / PACS, two temperature components are seen in CO rotational diagrams of Class 0/I. The median $T_{\rm rot}$ are ~ 320 K and ~ 690 K, for the 'warm' and 'hot' components, respectively, and do not correlate with physical parameters (bolometric luminosity and envelope mass). Such correlations are found for the total number of emitting CO molecules, in particular using the envelope mass, with the ratio of the hot-to-warm emitting molecules of order of 0.2. At the same time, however, the detection rate for the 'hot' component is significantly higher for the Class I sources, which have lower envelope masses.

The above results quantitatively agree with the interpretation proposed for the 'hot' CO component by Kristensen et al. (2013) who linked it to the 'medium' or 'offset' component extracted from the complex H_2O and CO profiles from HIFI and arising from dense ($n \sim 5 \times 10^4 - 10^6$ cm^{-3}) and hot ($T \sim 750$ K) gas in the inner 100 AU of the protostellar envelope (see also Kristensen et al. 2012). Comparison to shock models from Neufeld & Dalgarno (1989) implied an origin in a dissociative shock with the dissociation due to the UV radiation from the accreting protostar (see also Kristensen et al. in prep.). The 'hot' CO component would then trace the part of the shock where H_2 reforms (Kristensen et al. 2013).

The larger detection rate of the highly-excited CO lines in the more evolved sources from our study could be therefore related to the smaller shielding (wide-angle outflows, more dispersed envelopes) of UV radiation in the Class I sources rather than the higher dust continuum shielding opacity in the Class 0 sources. The detection of highly-excited H_2O lines in the sources with high$-J$ CO emission suggest the same origin during the embedded phase. In the Class II sources, where the envelope is fully dispersed, the hot H_2O emission and non-detections of high$-J$ CO argue in favor of the disk origin (Fedele et al. 2012, Riviere-Marichalar et al. 2012).

The 'warm component', on the other hand, traces the part of the shock that is more shielded from UV, probably further out along the outflow or deeper into the envelope. High absolute intensities of CO lines cannot be accounted by dissociative shocks alone and require the non-dissociative shock component (Karska et al. subm.).

5.5.2 Origin of [O I] emission: disk, jet, or UV-heated cavity walls?

A possible contribution from the disk to the [O I] 63 μm line is investigated via comparisons with more evolved, Class II sources. The envelope mass of Class II sources is negligible and the corresponding accretion / ejection rates are much lower compared to Class 0/I sources. Therefore, the contribution from the jet is expected to be low, with the bulk of [O I] emission originating in the disk.

Figure 5.1 shows our protostars on a diagram comparing the [O I] line emission with continuum at 63 μm with separate fits to the non-outflow Class II sources and Class II sources with associated jet emission taken from Howard et al. (2013)[3]. Not surprisingly, almost all of our sources are located above the 'non-outflow' fit and follow the fit to the 'outflow' Class II sources instead.

The relative contribution of the jet and / or UV–heated cavity walls to the total [O I]

---

[3] We note a mistake in equation 4 of Howard et al. (2013), which relates the [O I] line emission and continuum flux at 63 μm for the outflow sources, and not the non-outflow sources as claimed in the text. Based on their Figure 6, we obtained the equation for the non-outflow sources:

$$\log F([\mathrm{O\,I}]) = 0.737 \times \log(F_{\mathrm{cont}}) - 0.67 \tag{5.1}$$

where F([O I]) refers to the line flux of the [O I] 63 μm line in units of 10^{-16} W m^{-2} and F_{cont} to the continuum flux at 63 μm in Jy.

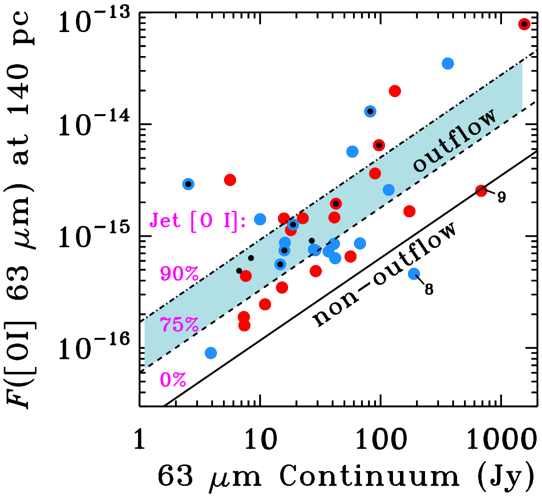

Figure 5.1 – Fluxes of the [O I] line at 63 μm as function of continuum flux at similar wavelength scaled to the common distance of 140 pc. The best fits to Class II sources in Taurus with jet / outflow emission (dashed line) and without (solid line) from Howard et al. (2013) are included for reference. Black dots denote sources with [C II] line detections (see Figure 5.6), three of them have less certain continuum values and as such have no corresponding blue / red circles. Sources lying on the dashed line have 25% contribution from the disk and 75% from the jet to the total [O I] emission, assuming that the solid line represents 100% contribution from the disk. The dash-dotted line represents sources with 90% jet contribution to [O I]. The shaded region denotes sources with 75% - 90% jet contribution to [O I] emission and includes the bulk of our sources.

emission can then be estimated assuming that the fit to the ‘non-outflow’ sources corresponds to the 100% emission coming from the disk. Accordingly, the sources on the ‘outflow’ fit have about 75% contribution from the jet / cavities to the [O I] flux, with a fraction of our sources showing more than 90% of these contributions (i.e. less than 10% contribution from the disk). As a consequence, we can rule out the disk emission to be an important factor influencing the [O I] emission observed in our protostars.

The excess [O I] emission is produced either in dissociative jet shocks, including a bow shock at the tip of the jet, or as a result of irradiation of outflow cavity walls by UV photons from these shocks and from a central protostar. A possible way to distinguish between the jet shocks and UV-heated cavity walls is to determine the densities of the emitting material. In the two-shock model, where the dissociative and non-dissociative shocks are assumed to be in a steady state, the higher-velocity jet shock propagates in smaller density material than the non-dissociative shock (Hollenbach 1997, Giannini et al. 2001).

For a subsample of our sources that show [C II] detections spatially associated with protostars, the analysis of PDR emission provides an independent measure of material densities that can be compared with densities for CO and H_2O excited in a non-dissociative shock. Since all of those sources have at least 75% of jet / cavities contribution to the [O I] emission (Figure 5.1), the corresponding gas densities are of order 10^4-$10^{5.5}$ cm^{-3} (Figure 5.6). The pre-shock densities obtained from the ratios of pairs of CO and H_2O lines are of similar order ($\sim 10^5$ cm^{-3}, Karska et al. subm, this work), but become larger by about a factor of 10 when the compression factor for a non-dissociative shock is accounted for. As a consequence, the densities in the outflow cavity shocks are too high to explain the [O I] emission, confirming a different origin in a dissociative jet shock for the considered subsample of sources.

Generally, the relative fraction of emission from the jet shocks and UV-heated cavity walls will likely differ depending on the evolutionary stage of a protostar and species considered. Large OH intensities relative to H_2O found in the Class I sources (Figures 5.2 and 5.A.1) indicate the increasing importance of H_2O photodissociating UV photons as a protostar evolves. At the same time, no such difference is seen between [O I] emission relative to H_2O in Class 0/I sources. In fact, both the total cooling in the [O I] lines (Figure 5.3) and the fraction of sources with detected high-velocity emission in the [O I] 63 μm line (Figure 5.1) is similar in Class 0 and I stages. On the other hand, if the [O I] emission is produced in a slower ($\upsilon \sim 15 - 40$ km s^{-1}), $C-$ or $J-$type shock, it should decrease for the more evolved sources with lower envelope masses (Figure 5.5). A combination of this effect with the larger amount of UV photons penetrating such a dispersed envelope in the Class I stage could provide an explanation to all our observations.

5.5.3 Mass flux rates: evidence for jet evolution?

The origin of the [O I] emission has consequences for the interpretation of the differences in the mass flux rates obtained from the low$-J$ CO and [O I] lines (§4.3). The [O I] mass flux rates are equal to $\sim 10^{-8}$ $M_\odot$ yr^{-1} for Class 0/I sources and as such are similar or up to an order of magnitude lower than the CO mass loss rates for the same sources (Figure 5.4).

The opposite result was obtained in Giannini et al. (2001), based on *ISO* observations of [O I] towards ~10 Class 0 sources. Here, the [O I] mass loss rates were comparable or higher to the CO rates, clearly because of the cloud contamination within a single beam. Some discrepancy between mass flux rates from CO and [O I] lines was seen in a subsample of our sources analyzed in Karska et al. (2013). In contrast to this preliminary study, however, no decrease in the [O I] luminosity is found from Class 0 to Class I stage (Figure 5.3 and Figure 5.3).

The mass flux rates from the [O I] line are calculated on the assumption that all [O I] emission is produced in the jet shock, which is most likely not the case. If indeed part of the [O I] emission is a product of H_2O photodissociation in a slower shock, the calculated rates are only upper limits to the actual mass loss rates, and differ even more from the CO 3-2 and 6-5 rates, in particular for the more evolved sources. In such more evolved sources, the outflow cavity has widened and emptied, resulting in less efficient entrainment.

Interestingly, the majority of the sources with low CO / [O I] mass flux ratios are the more evolved Class I sources (Figure 5.4). Bright [O I] jets are also seen in Class II sources (Podio et al. 2012), where much weaker CO wind mass flux rates are found. In contrast, the most deeply embedded sources have large CO / [O I] mass flux ratios suggesting that [O I] underestimates the momentum flux, perhaps because the jet is partly molecular (Nisini et al. in prep.).

Altogether, this shows a possible evolution of the wind: in the most deeply embedded stages the jet is mostly molecular and evolves to the more atomic form as the envelope is dissipated, the outflow cavities widen, and the gas entrainment is reduced. Velocity-resolved observations of [O I] are needed to determine the relative jet and UV contributions and thus the details of the jet evolution.

5.6 Summary and conclusions

Herschel / PACS observations of hot gas in the surroundings of low-mass protostars allow to disentangle and characterize energetic physical processes associated with the earliest stages of star formation. CO and H_2O line are primary tracers of non-dissociative shocks occurring in the outflows on 10^3-10^4 AU scales. Dissociative shocks due to the fast-moving jet and H_2O photodissociation by UV photons contribute to the [O I] emission. The [C II] line is a unique tracer of the UV strength when spatially associated to a young protostar. The main conclusions are the following:

1. Two temperature components are found on CO diagrams, with $T_{\rm rot} \sim 320$ K and ~ 690 K. Although the number of emitting molecules in the two components correlates with the envelope mass, the detection rates of the hot component are significantly lower for the Class 0 sources. These results are consistent with the interpretation proposed by Kristensen et al. (in prep.) that the hot component originates in a dissociative shock exposed to protostellar UV photons. The warm component, on the other hand, originates in non-dissociative shocks to account for the high absolute intensities of CO lines. The highly-excited H_2O line is most probably related to the same physical component.

2. Similar to previous studies, the CO molecular cooling over bolometric luminosity ratio is larger for the Class 0 sources. The total cooling in the [O I] line, on the other hand, is the same for Class 0/I sources, contrary to the *ISO* results from Nisini et al. (2002b). The contribution from the disk to the [O I] emission is negligible for the deeply-embedded protostars considered here. The [O I] flux originates in the jet shocks and in the UV irradiated cavity walls where H_2O photodissociates. The fraction of the jet emission decreases for more evolved sources, but the penetration by UV photons is enhanced, explaining a similar amount of [O I] cooling in Class 0/I sources.

3. Incident UV field and densities are calculated for a subsample of sources with detected [C II] emission using the Kaufman et al. (1999) models of photodissociation

regions. UV fields of $\sim 10-100$ G_0 and densities of $n \sim 10^4-10^{5.5}$ cm^{-3} are determined. The densities are an order of magnitude lower than the values obtained from comparison of molecular emission to shock models indicating the origin inside the outflow cavities.

4. Mass flux rates in the jet/wind of order $\sim 10^{-8}$ $M_\odot$ yr^{-1} are calculated from the [O I] 63 μm line for both Class 0 and I sources. Those values are similar or up to an order of magnitude lower than the wind mass flux rates inferred from CO using momentum conservation and obtained for the same sources in a uniform manner. Differences are found between Class 0 and I sources, with the latter showing the [O I] mass flux rates exceeding the CO rates, suggesting that the atomic component of the jet dominates.

Acknowledgements

Herschel is an ESA space observatory with science instruments provided by the European-led Principal Investigator consortia and with important participation from NASA. Astrochemistry in Leiden is supported by the Netherlands Research School for Astronomy (NOVA), by a Royal Netherlands Academy of Arts and Sciences (KNAW) professor prize, by a Spinoza grant and grant 614.001.008 from the Netherlands Organisation for Scientific Research (NWO). Support for this work, part of the Herschel Open Time Key Project Program, was provided by NASA through an award issued by the Jet Propulsion Laboratory, California Institute of Technology.

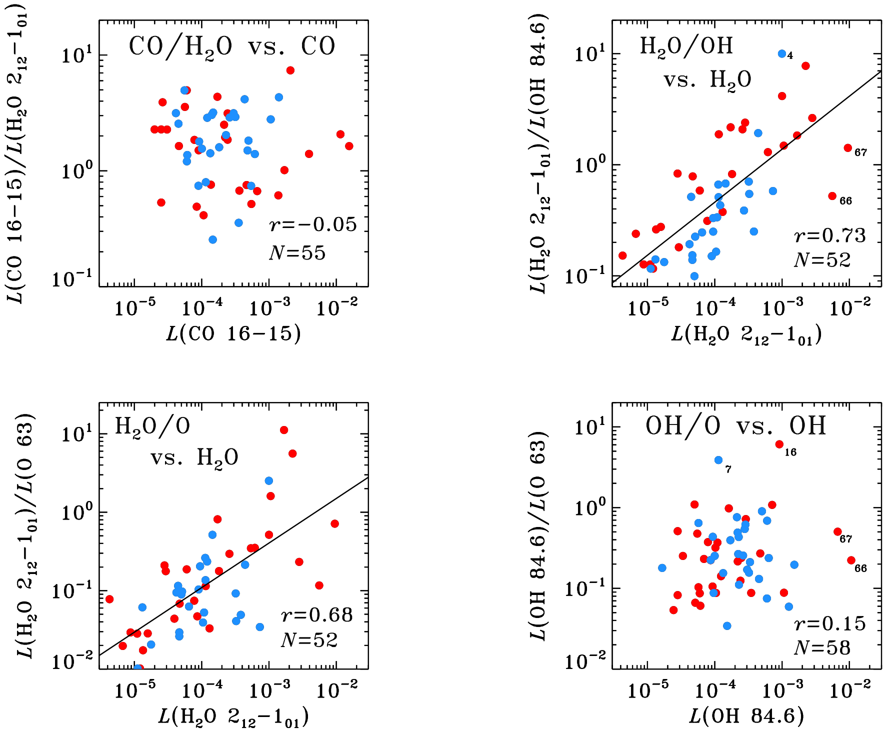

Figure 5.A.1 – Flux ratio - flux correlations between the CO 16-15 / H_2O 2_{12}-1_{01} and CO 16-15 lines (top left), the H_2O 2_{12}-1_{01} / OH 84.6 μm and H_2O 2_{12}-1_{01} lines (top right), the H_2O 2_{12}-1_{01} / [O I] 63 μm and H_2O 2_{12}-1_{01} lines (bottom left), and the OH 84.6 μm / [O I] 63 μm and OH 84.6 μm lines. Class 0 sources are shown in red and Class I sources in blue. Correlation coefficients (r) and number of sources with line detections (N) are shown on the plots. Solid lines show the best linear fits obtained with a least-squares method for cases where the correlation coefficient exceeds the 3σ threshold.

Appendix

5.A Correlations of fluxes and flux ratios

Figure 5.A.1 shows correlations between line ratios of different species as functions of line fluxes of one of those species. Strong, $\sim 5\sigma$ correlations are found between the H_2O 2_{12}-1_{01} / OH 84.6 μm ratio and the H_2O 2_{12}-1_{01} flux and between the H_2O 2_{12}-1_{01} / [O I] 63 μm ratio and the H_2O 2_{12}-1_{01} flux.

Table 5.B.1 – Correlation coefficients for line fluxes and sources parameters relations

	$L_{\rm bol}$		$M_{\rm env}$	
	r	N	r	N
CO 16-15	**0.56**	70	**0.60**	57
CO 29-28	0.53	46	0.55	39
H_2O 2_{12}-1_{01}	0.45	57	**0.75**	47
H_2O 2_{21}-1_{10}	0.54	52	**0.72**	44
OH 84 μm	**0.58**	62	0.44	49
O I 63 μm	**0.65**	70	0.47	56

Notes. All correlation coefficients exceed the 3 σ threshold values, the ones exceeding the 4 σ threshold are shown in boldface.

5.B Correlations with sources parameters

Figures 5.B.1 and 5.B.2 illustrate how line luminosities of molecules and [O I] correlate with two main physical parameters of the sources: bolometric luminosities and envelope masses. The correlations with source bolometric luminosities are particularly strong for the [O I] and OH lines (see Table 5.B.1) and to a smaller extent with the CO 16-15 line. Lack of correlation is found for H_2O and higher$-J$ CO transitions.

The envelope masses, on the other hand, correlate most strongly with the H_2O lines (at 5σ level) and CO 16-15 line (at 4.5σ level). In the sub-thermally excited H_2O lines this could be just an excitation effect, however a strong correlations with the CO line and the decrease of line with of H_2O lines for the Class I sources (Mottram et al. submitted) indicate that evolution also plays a role.

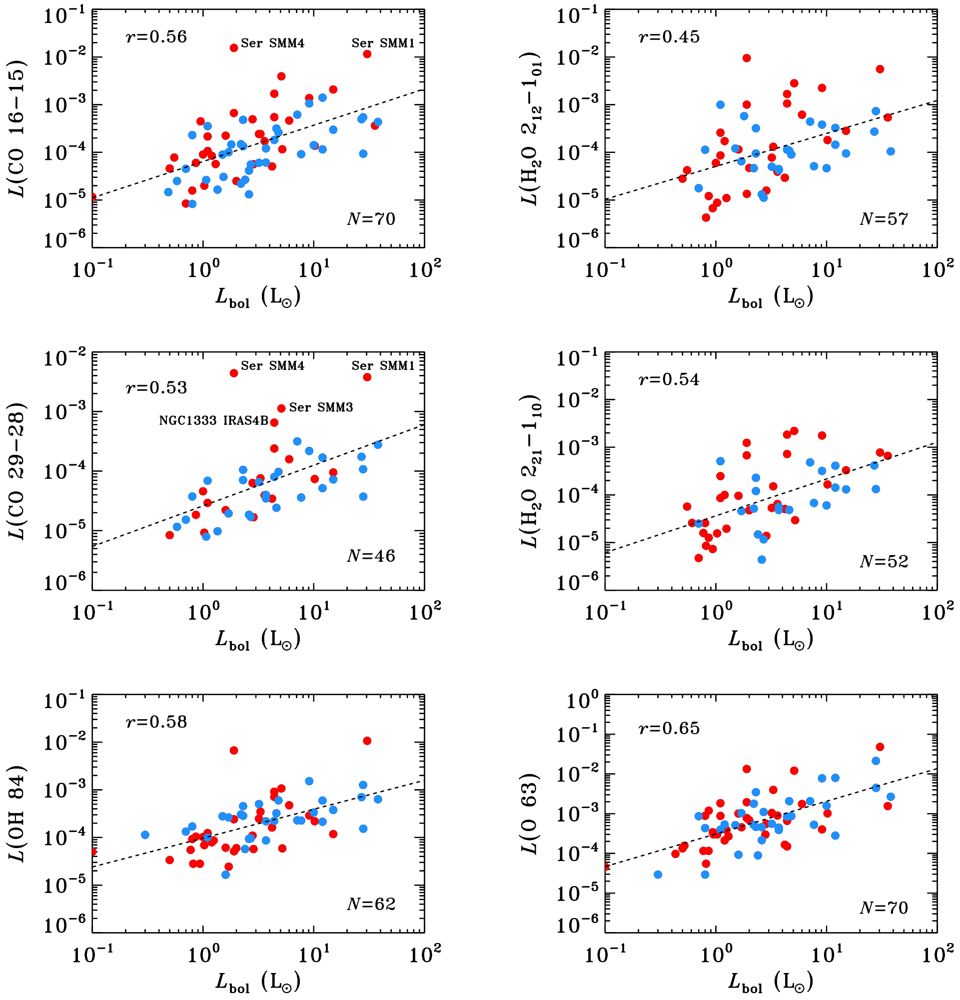

Figure 5.B.1 – Correlations of source bolometric luminosity and line fluxes of CO 16-15, CO 29-28, H_2O 2_{12}-1_{01}, H_2O 2_{21}-1_{10}, OH doublet at 84 μm, and [O I] line at 63 μm. Correlation coefficients (r) and number of sources with line detections (N) are shown on the plots and in Table 5.B.1.

5.C Rotational diagrams for the WILL sources

Figures 5.C.1 and 5.C.2 show CO rotational diagrams for the WILL sources. Separate linear fits are done to the transitions located in the 'warm' and 'hot' components, the same as used in Karska et al. (2013) and Green et al. (2013). Figures 5.C.3 and 5.C.4 show H_2O rotational diagrams with only one linear fit to all observed lines.

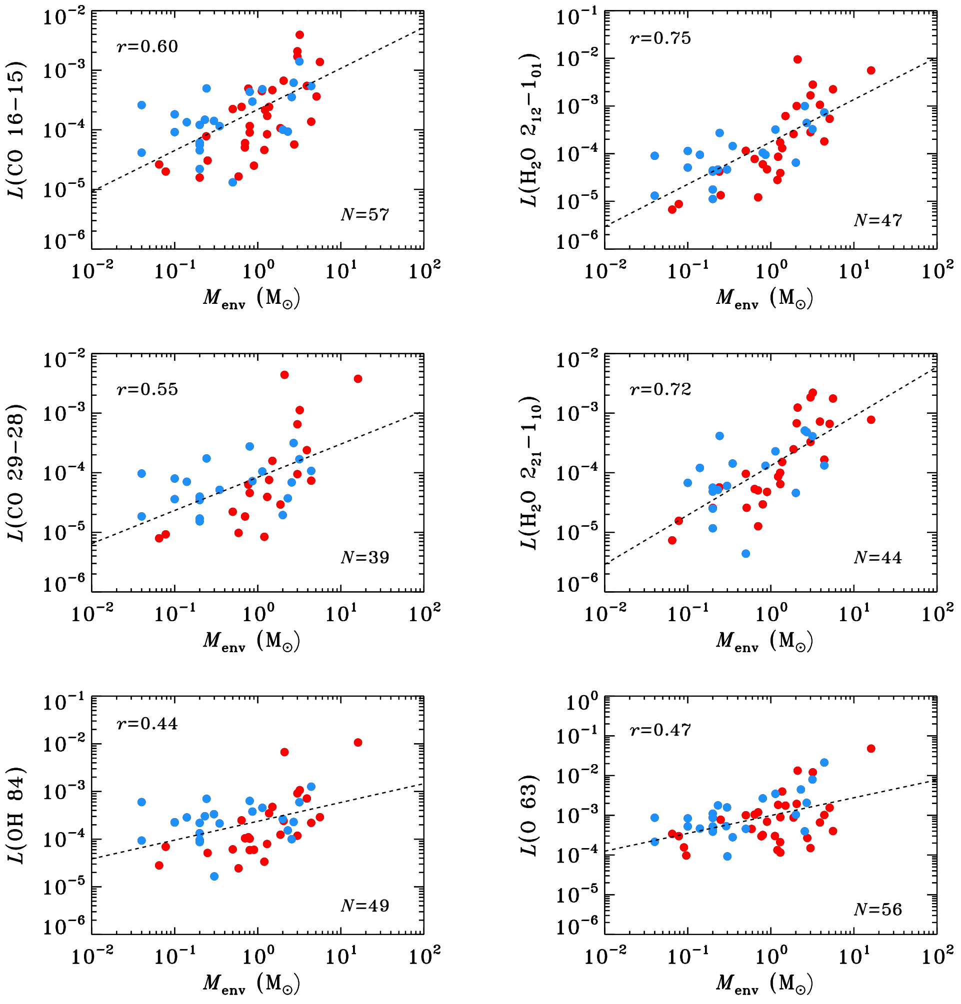

Figure 5.B.2 – Similar to Figure 5.B.1, except that the line fluxes are correlated with envelope masses.

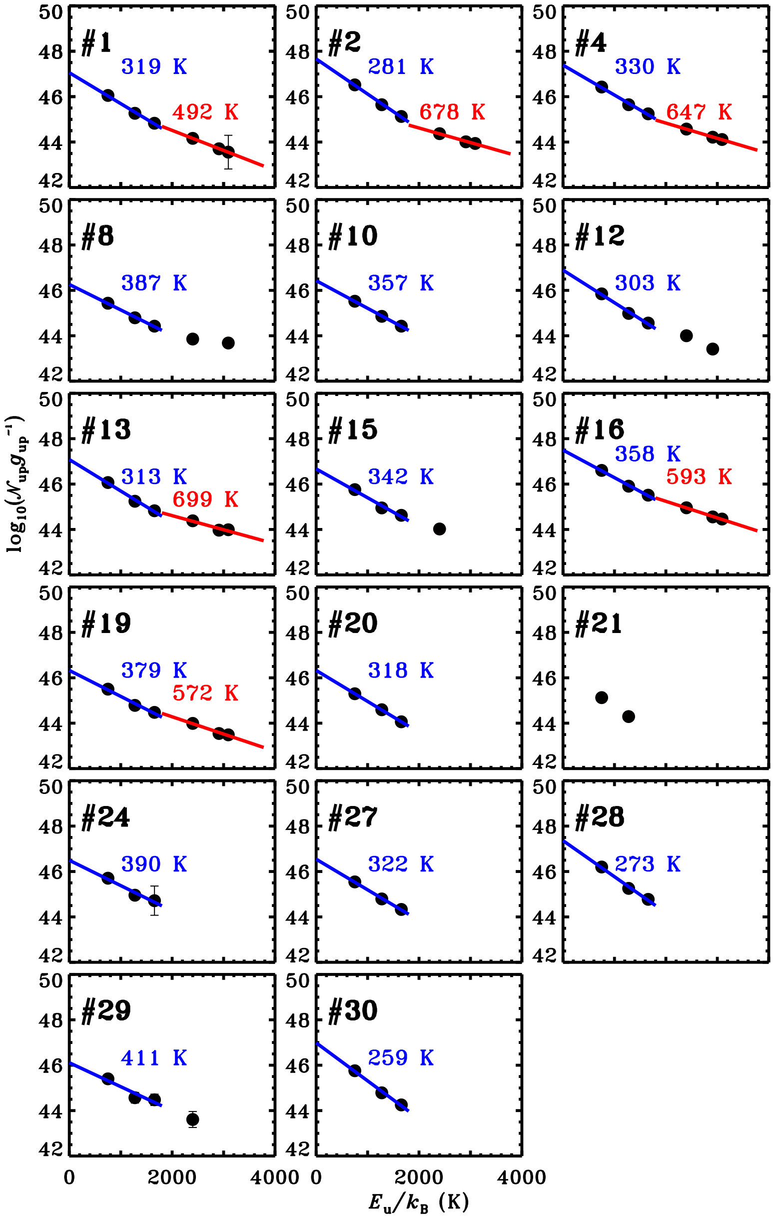

Figure 5.C.1 – Rotational diagrams of CO for Perseus sources not included in Karska et al. (2013) and Green et al. (2013). The base-10 logarithm of the number of emitting molecules from a level u, $\mathcal{N}_{\rm u}$, divided by the degeneracy of the level, $g_{\rm u}$, is shown as a function of energy of the upper level in kelvins, $E_{\rm up}$. Blue and red solid lines show linear fits to the data and the corresponding rotational temperatures, when at least 3 lines are detected.

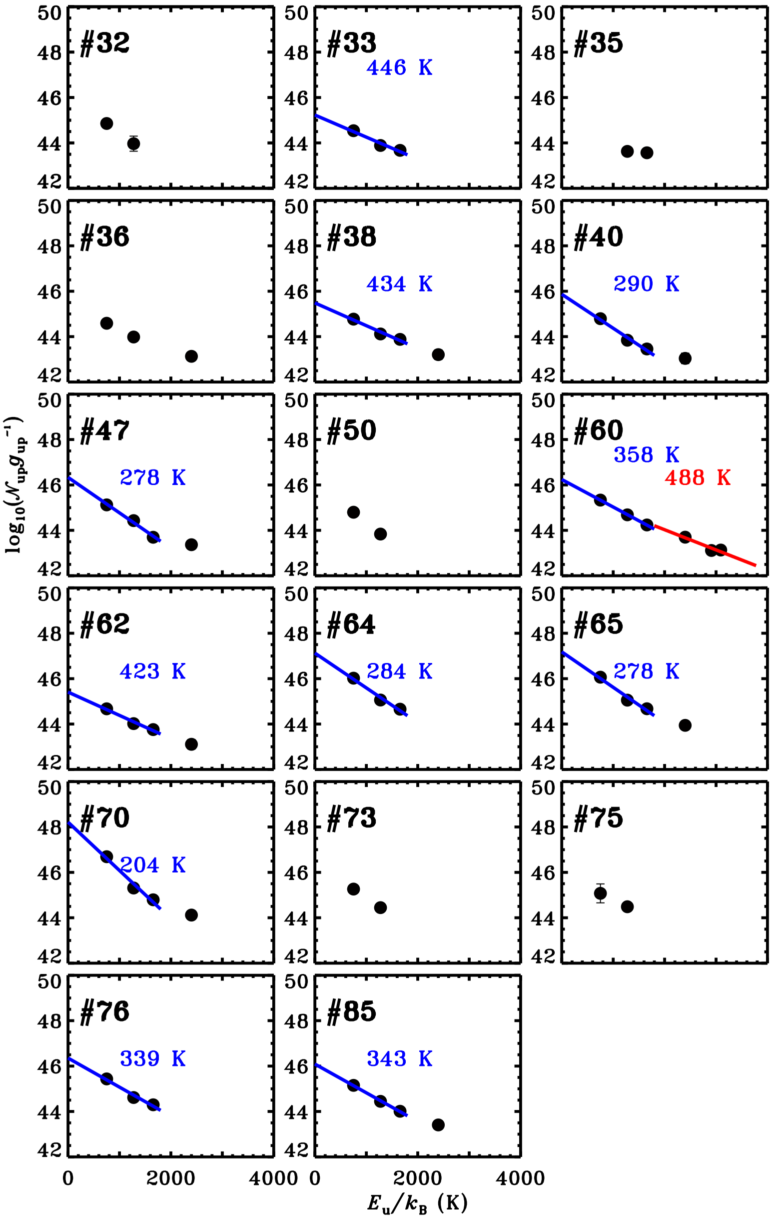

Figure 5.C.2 – The same as Figure 5.C.1, but for the remaining sources from the WILL program.

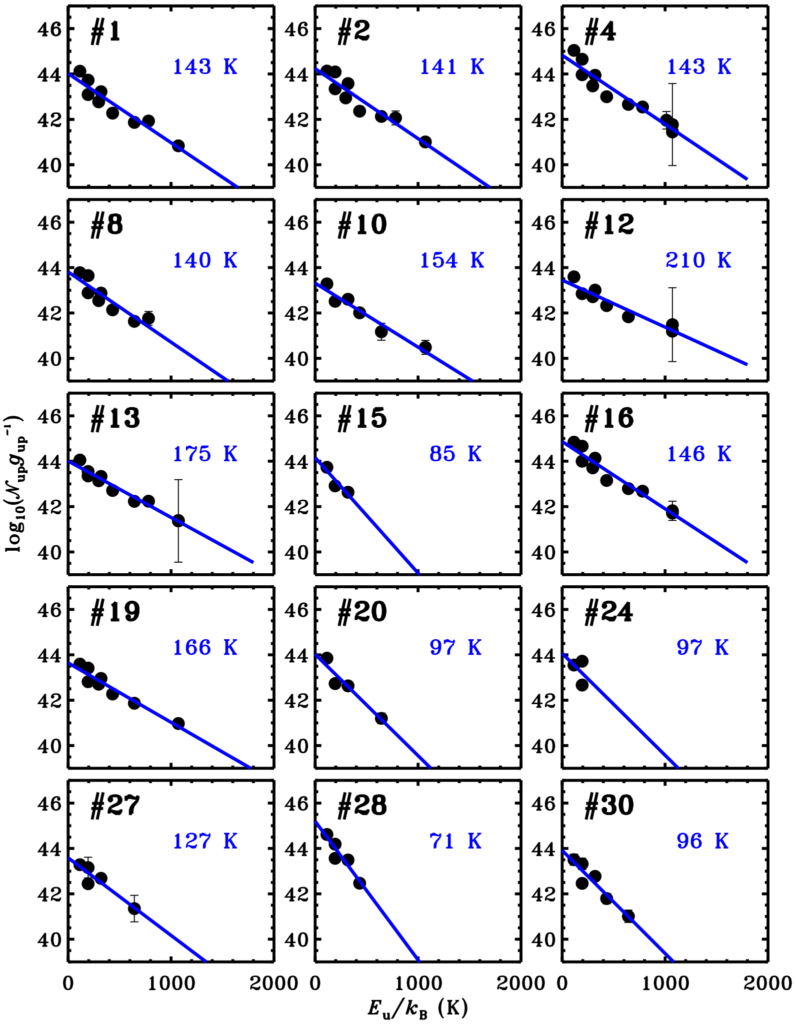

Figure 5.C.3 – Rotational diagrams of H_2O for Perseus sources not included in Karska et al. (2013) and Green et al. (2013).

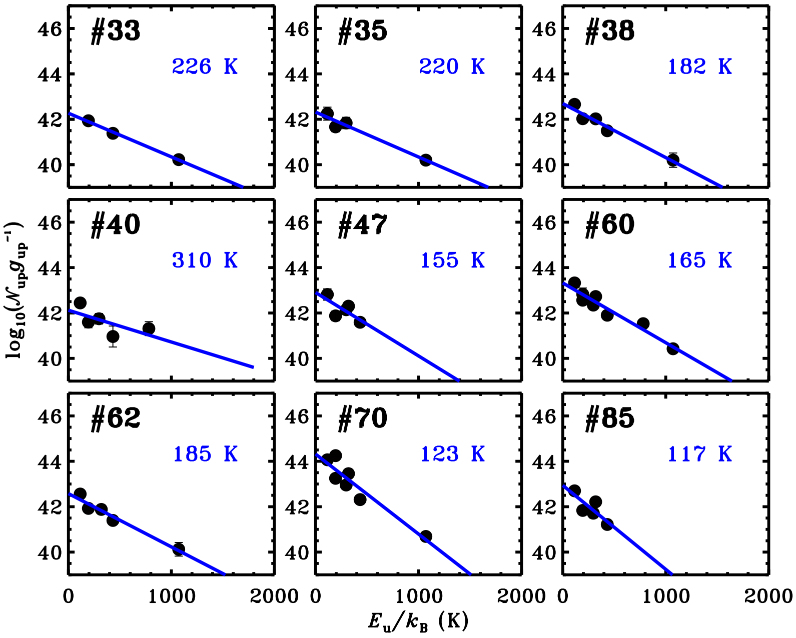

Figure 5.C.4 – The same as Figure 5.C.3, but for the remaining sources from the WILL program.